



Flux Ropes, Turbulence, and Collisionless Perpendicular Shock Waves: High Plasma Beta Case

G. P. Zank¹ , M. Nakanotani² , L. L. Zhao³ , S. Du⁴ , L. Adhikari² , H. Che¹ , and J. A. le Roux¹ 

¹ Center for Space Plasma and Aeronomic Research (CSPAR) Department of Space Science University of Alabama in Huntsville Huntsville, AL 35805, USA
garyp.zank@gmail.com

² Center for Space Plasma and Aeronomic Research (CSPAR) University of Alabama in Huntsville Huntsville, AL 35805, USA

³ Department of Space Science University of Alabama in Huntsville Huntsville, AL 35805, USA

⁴ Los Alamos National Laboratory Los Alamos, NM 87545, USA

Received 2021 January 7; revised 2021 April 9; accepted 2021 April 12; published 2021 June 3

Abstract

With the onset of solar maximum and the expected increased prevalence of interplanetary shock waves, Parker Solar Probe is likely to observe numerous shocks in the next few years. An outstanding question that has received surprisingly little attention has been how turbulence interacts with collisionless shock waves. Turbulence in the supersonic solar wind is described frequently as a superposition of a majority 2D and a minority slab component. We formulate a collisional perpendicular shock-turbulence transmission problem in a way that enables investigation of the interaction and transmission of quasi-perpendicular fluctuations such as magnetic flux ropes/islands and vortices as well as entropy and acoustic modes in the large plasma beta regime. We focus on the transmission of an upstream spectrum of these modes, finding that the downstream spectral amplitude is typically increased significantly (a factor of 10 or more), and that the upstream spectral index of the inertial range, and indeed the general spectral shape, is unchanged for the downstream magnetic variance, kinetic energy, and density variance. A comparison of the theoretically predicted downstream magnetic variance, kinetic energy, and density variance spectra with those observed at 1, 5, and 84 au by Wind, Ulysses, and Voyager 2 shows excellent agreement. The overall theoretically predicted characteristics of the transmission of turbulence across shocks observed in the solar wind appear to be largely consistent with recent observational studies by Pitňa et al. and Borovsky.

Unified Astronomy Thesaurus concepts: [Interplanetary shocks \(829\)](#); [Interplanetary turbulence \(830\)](#)

1. Introduction

Despite its importance to particle acceleration via diffusive shock acceleration, the perhaps more pedestrian interaction of magnetized turbulence with interplanetary shocks has attracted insufficient attention even though in situ observations are relatively abundant. In this first of a series of papers, we begin to explore systematically the interaction of magnetohydrodynamic (MHD) turbulence with shocks that are typical of solar wind conditions, including the heliospheric termination shock (HTS). Of particular interest are the spectral characteristics of the transmitted turbulence field. Perhaps the earliest such study was that of Luttrell & Richter (1987) who investigated upstream and downstream magnetic field and density spectra in the frequency range 10^{-4} – 10^{-2} Hz for parallel forward sub- and supercritical interplanetary shocks, also identifying Alfvén and magnetosonic modes in the data. Subsequent related studies by Kallenbach et al. (2005), Li et al. (2005), Zank et al. (2006), Bamert et al. (2008), Hu et al. (2012) found that the downstream power in the turbulent field was typically an order of magnitude larger than the power in the upstream field. Hu et al. (2013) furthermore found that the fluctuations were predominantly transverse and that Alfvén waves were found immediately upstream of quasi-parallel shocks. Zank et al. (2006), in their study of quasi-perpendicular interplanetary shocks, found little evidence of upstream wave activity unless the shock was quasi-parallel. Pitňa et al. (2016) provide an important new study of the interaction of plasma turbulence interacting with interplanetary shocks over a frequency range that extends from MHD to kinetic scales. We focus primarily on their results in the MHD regime. By

using ion flux fluctuations as a proxy for density fluctuations, Pitňa et al. (2016) explored the spectra upstream and downstream of oblique, fast-mode forward interplanetary shocks, thereby providing a useful complement to prior studies that focus on the transmission of magnetic field fluctuations. The two MHD scale conclusions that emerge from Pitňa et al. 2016 are that the intensity of ion flux fluctuations is larger by an order of magnitude downstream than upstream for most shocks investigated, and that the spectral indices upstream and downstream are essentially unchanged with a correlation coefficient of about 0.75. Subsequently, Pitňa et al. (2017) investigated the downstream decay of magnetic and kinetic energy, finding consistency with basic MHD turbulence decay laws. Interestingly, Pitňa et al. (2017) find that the downstream turbulence decay begins some distance behind the shock. A 2D hybrid simulation by Nakanotani et al. (2020) indicates that the interaction of multiple current sheets with a shock wave results in magnetic reconnection developing further downstream due to the tearing instability with the resultant development of turbulent electromagnetic fields. The Pitňa et al. and related results are well reviewed by Pitňa et al. (2021). The interaction of Alfvénic fluctuations with a quasi-perpendicular shock yielded an enhanced downstream spectrum some 10–30 times larger than that upstream (Lu et al. 2009). In related work, Adhikari et al. (2016a, 2016b) applied the large plasma beta turbulent transport model of Zank et al. (2012) to examine the transport of incompressible turbulence across quasi-parallel and quasi-perpendicular interplanetary shocks. The theoretical results yielded an increase in turbulent energy across the shock, but not by a very large factor. In related work, Zank et al. (2018)

used a nearly incompressible (NI) formulation to explore the transmission of incompressible turbulence across the HTS, finding that the majority 2D component is more amplified across the shock compared to the minority slab component. The normalized residual energy increases across the HTS, changing from a state nearly equilibrated in kinetic and magnetic energy density to one in which the downstream kinetic energy dominates. Borovsky (2020) investigated statistically the upstream and downstream fluctuation properties of 109 strong forward propagating interplanetary shocks. The study distinguishes between four types of solar wind plasma according to its origin. In a sense, the distinction between the different types of plasma introduced by Borovsky (2020) may represent a proxy for the dominant characteristics of the upstream fluctuations. Unfortunately, the study did not distinguish between shock obliquity despite its fundamental importance to shock structure and upstream wave activity. A superposed-epoch analysis was performed on the upstream and downstream states. Borovsky (2020) finds that the downstream fluctuating magnetic field variance and kinetic energy spectra are slightly steeper than those upstream, and that the steepening in the kinetic energy spectra is greater than that in the magnetic field variance. Furthermore, the upstream velocity and magnetic field fluctuations are amplified on transmission through the shock, and are correlated across the shock. The fluctuating Alfvén ratio $r_A = \delta u^2 / (\delta B^2 / \mu_0 \rho)$ (δu and δB the fluctuating velocity and magnetic field, respectively, ρ the plasma density, and μ_0 the magnetic permeability) decreases across the shock, as does the cross helicity. Finally, in what Borovsky 2020 describes as the plasma inhomogeneity or *lumpiness* $\delta\rho/\rho$ and $\delta B/B$ increase from upstream to downstream of the shock.

In this series of papers, we retreat somewhat from the nonlinear but incompressible models of Adhikari et al. (2016a, 2016b) and Zank et al. (2018) and explore the interaction of turbulence with shocks from both a linear theoretical and observational perspective, initiated in large part by the rather detailed observations of Pitňa et al. (2016, 2017) and Borovsky (2020). The solar wind is a mix of Alfvénic fluctuations, pressure balanced structures, and magnetic flux ropes separated by current sheets, the last typically being the dominant component (e.g., Borovsky 2010; Li et al. 2011; Borovsky & Burkholder 2020). We focus on the energy-containing and inertial range of magnetized solar wind turbulence, allowing us to utilize an MHD description. A current model for turbulence in the solar wind is that it is a superposition of a majority quasi-2D component and a minority slab component (Zank & Matthaeus 1992, 1993; Bieber et al. 1996; Forman et al. 2011; Adhikari et al. 2017a, 2017b; Zhao et al. 2017; Zank et al. 2017a, 2020). From this perspective, it is important therefore to explore the interaction of flux ropes with shock waves since low-frequency turbulence in the solar wind is dominated by quasi-2D structures and slab turbulence represents only a minority component. We do not consider kinetic scale turbulence.

Although the transmission of MHD waves across shocks has been quite widely investigated theoretically (see for example the still excellent summary in Anderson (2003) that discusses the early investigations), including in the context of diffusive shock acceleration (e.g., Achterberg & Blandford 1986; Campeanu & Schlickeiser 1992; Vainio & Schlickeiser 1998) and the transmission of Alfvén waves through a shock (McKenzie & Westphal 1969), many aspects of the problem

remain open, particularly in terms of understanding the spectral characteristics of the transmitted fluctuations such as flux ropes. In regard to diffusive shock acceleration, we note but do not address the interesting work related to the significant amplification of magnetic fields at strong, fast shocks by, e.g., Giacalone & Jokipii (2007), Guo et al. (2012), and Frascchetti (2013), nor do we consider the back-reaction of turbulence on shocks (Scholer & Belcher 1971; McKenzie & Bornatici 1974; Vainio & Schlickeiser 1999; Zank et al. 2002).

In this paper, we address a problem that appears not to have been discussed very much theoretically despite its relevance to several heliospheric problems. Specifically, we consider a shock geometry for which there exists a mean magnetic field \mathbf{B}_0 , oriented perpendicularly to the shock normal and obliquely to the flow velocity vector. We will assume that the plasma beta $\beta_p = P / (B_0^2 / 2\mu_0)$ is large. Here, $P = 2n_p k T_p$, where n_p and T_p are the proton number density and temperature, respectively, and k Boltzmann’s constant. As illustrated in Figure 1 (left), the shock itself can be thought of as a 2D locally planar structure such that in the solar wind, the velocity vector \mathbf{U} is oriented obliquely to the shock front, and beyond several astronomical units, the magnetic field \mathbf{B} is azimuthal—roughly orthogonal to the radial flow \mathbf{U} and in the plane of the shock. In the cartoon (left), two possible orientations of the shock geometry for the MHD Rankine–Hugoniot conditions are shown. In the typical orientation, the 1D shock is generally taken as the black wiggly curve parallel to the magnetic field \mathbf{B} , i.e., in the plane of the flow velocity and magnetic field vector. However, one can equally choose the second orientation (the blue wiggly curve in the cartoon), which is orthogonal to both \mathbf{U} and \mathbf{B} . As we show below, the mean field equations admit the same perpendicular Rankine–Hugoniot conditions for both shock orientations. However, the shock geometry of the latter allows one to examine more easily the interaction of fluctuations that are 2D in a plane orthogonal to the mean magnetic field with the shock than the other. We further assume that the mean magnetic field is relatively weak in the sense that magnetic fluctuations are of the same order as \mathbf{B}_0 . This might also be interpreted as a strong magnetic turbulence limit. Although certainly idealized, the formulation of the problem allows us to examine the interaction of magnetic flux ropes with a shock in a novel way. The geometry is appropriate to shocks propagating in the more distant solar wind beyond a few astronomical units, including the HTS. Furthermore, in the inner heliosphere, this geometry is likely to be suitable for regions of shocks that are quasi-perpendicular (Figure 1, right) and the assumption of a weak mean field allows one to consider shock propagation in the region of the heliospheric current sheet (HCS; Figure 1, bottom). Hence, in this paper, we consider the blue shock orientation, which allows us to examine the magnetic island wave mode. The black shock, although also a perpendicular shock, is suitable for Alfvén wave transmission.

Although $\beta_p \simeq 1$ or < 1 in much of the supersonic solar wind, there are regions where $\beta_p \geq 1$. In particular, beyond the ionization cavity, the creation of pickup ions results in the solar wind plasma satisfying $\beta_p > 1$, and upstream of the HTS, $\beta_p \simeq 4$ (Zank et al. 2018). Thus, the plasma beta for shocks propagating in the supersonic solar wind beyond some 8 au will be large. Furthermore, downstream of the HTS, Zhao et al. 2019b identified a set of magnetic flux ropes finding that these were sites of anomalous cosmic-ray proton acceleration, suggesting that flux ropes interacted with the HTS and were

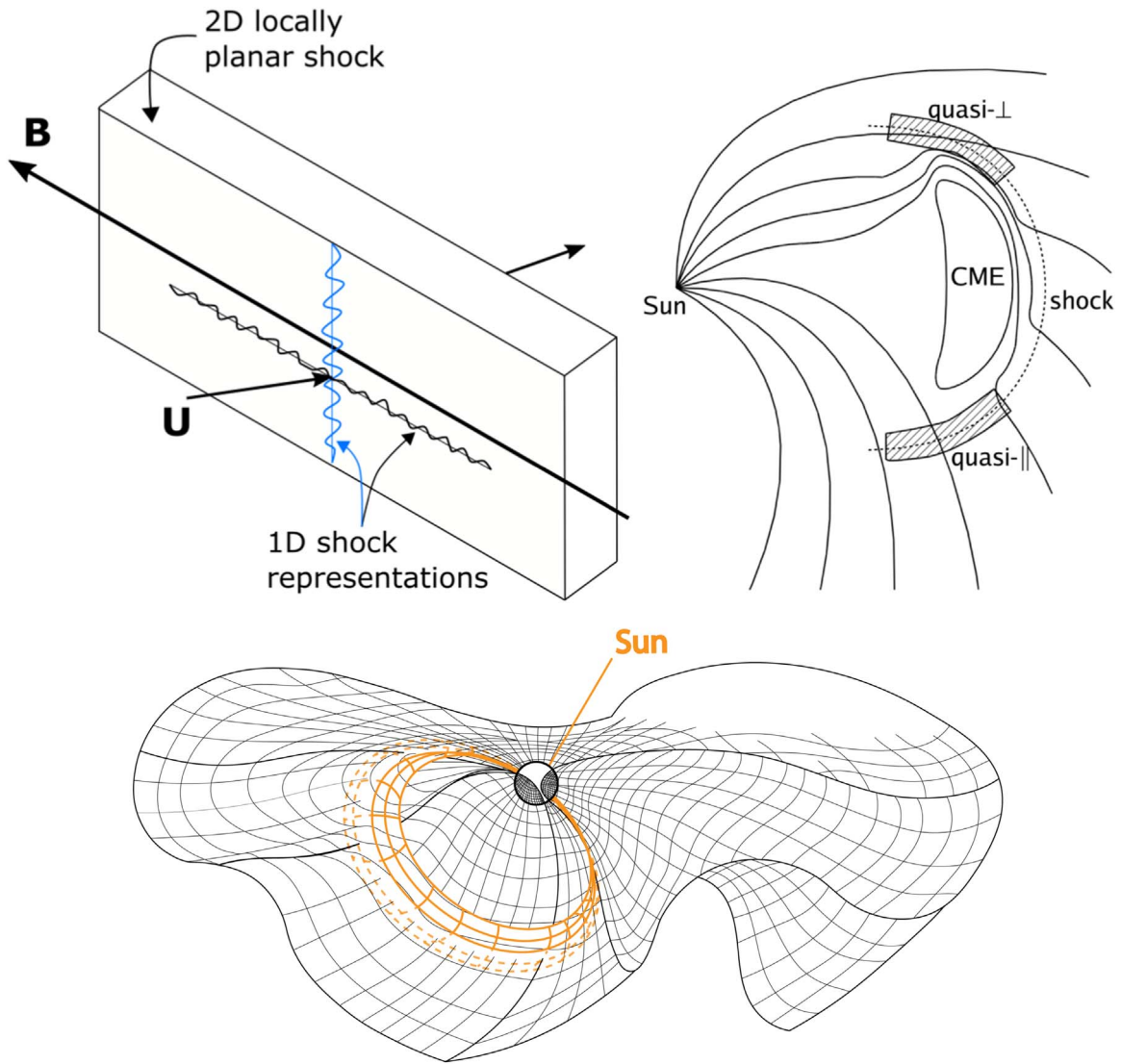


Figure 1. Top left: geometry of a perpendicular shock in the solar wind. The block identifies a section of a shock front on a scale that renders it locally planar. The magnetic field vector lies in the plane of the shock front (perpendicular to the shock normal), and the incident upstream flow vector is oblique to the shock front. Two possible reductions to a 1D shock geometry that preserve a perpendicular configuration are possible, as illustrated by the black and blue wiggly lines. In this paper, we consider the blue shock orientation, which allows us to examine the magnetic island wave mode. The black shock, although also a perpendicular shock, is suitable for Alfvén wave transmission. Top right: illustration of the quasi-perpendicular region of a coronal mass ejection (CME)-driven shock in the inner heliosphere for which the shock geometry at the left can be applied. Bottom: cartoon illustrating the interaction of an ecliptic CME-driven shock wave with the HCS. The Sun is in the center and the black curves depict the wavy HCS and the orange curved structure shows the shock wave propagating and intersecting the HCS. Solid lines indicate regions of the shock above the HCS and orange dashed lines indicate below the HCS.

transmitted downstream. Besides pickup ions, energetic particles accelerated diffusively at a shock, such as CME events associated with gradual particle events, can contribute to the local upstream and downstream pressure (Zank et al. 2014a; Mostafavi et al. 2018; Zank et al. 2018). In these cases, even if the plasma beta associated with the thermal background plasma is $O(1)$ or smaller, the inclusion of energetic ions or pickup ions will make the total plasma beta larger. The relatively tenuous population of suprathermal particles contributes to the total pressure but, other than in driving turbulence, they appear to play little role in the development and evolution of MHD turbulence, with the result that the basic solar wind superposition of quasi-2D and slab fluctuations model remains valid even in the vicinity of high plasma beta shock waves. Finally, we note that the derivation of the pressure in the MHD

description includes contributions from all particle species (protons, electrons, and energetic particles) and consequently, the total plasma beta can exceed 1 frequently.

As illustrated in the cartoon, Figure 1 (bottom), a shock wave driven off the Sun in the ecliptic will propagate through and intersect the wavy HCS. So too will interplanetary shocks formed as a result of fast stream–slow stream interactions. The HCS identifies the change in polarity of the interplanetary magnetic field, extending throughout the equatorial plane of the heliosphere, including the inner heliosheath beyond the HTS (e.g., Zank 2015), and possesses a complex 3D wavy (*ballerina skirt*) structure with an opening angle that varies with solar cycle. The presence of oppositely oriented magnetic field results in a highly dynamical structure that is likely neither contiguous nor continuous. In the vicinity of the HCS, the

magnetic field strength drops significantly and the solar wind density increases, yielding a larger plasma beta β_p than is typical of the rest of the solar wind (observed values of β_p in the vicinity of the HCS can often substantially exceed 1). Recurrent magnetic reconnection expected to occur in the presence of strong current sheets experiencing driving by the variable solar wind is thought to produce the numerous flux ropes observed in the vicinity of the HCS (Moldwin et al. 2000; Eastwood et al. 2002; Cartwright & Moldwin 2010; Eriksson et al. 2014; Yu et al. 2014; Khabarova et al. 2015a, 2015b, 2016; Khabarova & Zank 2017; Hu et al. 2018; Zheng & Hu 2018; Chen et al. 2019; Malandraki et al. 2019; Zhao et al. 2019a). Indeed, the possibility that reconnection might spawn small-scale secondary current sheets, fluctuations, and waves and multiscale magnetic islands has been discussed widely (Khabarova & Zastenker 2011; Bárta et al. 2011a, 2011b; Guo et al. 2014; Osman et al. 2014; Zhou et al. 2015; Li et al. 2017, 2018; Guo et al. 2016; Du et al. 2018, 2020; Che & Zank 2020). Flux ropes, also known as magnetic islands, are present ubiquitously in the solar wind. They have been found downstream of the HTS (Zhao et al. 2019b) and deep in the inner solar wind (Zhao et al. 2020b, 2020a). Flux ropes occur across an enormous range of scales, most likely reflecting their different possible origins, from magnetic clouds associated with CMEs that have scales sizes exceeding 0.1 au down to sizes less than 0.006 au (e.g., Moldwin et al. 2000; Eastwood et al. 2002; Khabarova et al. 2015a; Hu et al. 2018; Zheng & Hu 2018; Zhao et al. 2019a, 2020b). Figure 1 of Khabarova et al. (2015a) shows that small-scale flux ropes are clustered in close proximity to the HCS (see also Eastwood et al. 2002; Eriksson et al. 2014). The highly dynamical character of magnetic islands in the vicinity of the HCS was revealed further by observations of merging flux ropes reported by Khabarova et al. (2015a) and Hu et al. (2018).

Zhao et al. 2019a describe an interplanetary shock wave at ~ 5 au in the vicinity of the HCS, and numerous magnetic islands are observed for some distance in both the upstream and downstream regions. The downstream region appeared to be responsible for accelerating protons to high energies, and the observed energetic particle distribution function was well described by a transport theory (Zank et al. 2014b; Zhao et al. 2018) for particle acceleration by dynamically interacting magnetic islands and turbulent reconnection-related processes (Zhao et al. 2019a). This raises the important question of how a shock in the vicinity of the HCS interacts with upstream turbulence and structures and if that interaction is responsible for enhancing the production and amplification of flux ropes behind the shock wave, and does this then contribute directly to the subsequent acceleration of charged particles further downstream as suggested by Zank et al. (2015) and le Roux et al. (2016)?

In this paper, we present a theoretical model in Section 2 that describes the linear interaction of upstream vortices, magnetic flux ropes or islands, entropy, and acoustic fluctuations with a perpendicular shock wave in a high plasma beta environment. In Section 3, we provide solutions to the transmission equations and consider different incident fluctuations, examining the transmission and generation of downstream modes and spectra. Finally, in Section 4 we present observations and a comparison of theory to the spectra of three shocks located at 1, 5, and 84 au. Conclusions and further discussion can be found in Section 5.

2. Interaction of Magnetized Structures with a Shock Wave

The conservation form of the MHD equations that are needed to derive the appropriate boundary conditions (BCs) at the shock are given by

$$\frac{\partial \rho}{\partial t} + \nabla \cdot (\rho \mathbf{U}) = 0; \quad (1)$$

$$\frac{\partial}{\partial t}(\rho \mathbf{U}) + \nabla \cdot \left[\rho \mathbf{U} \mathbf{U} + \left(P + \frac{B^2}{2\mu_0} \right) \mathbf{I} - \frac{1}{\mu_0} \mathbf{B} \mathbf{B} \right] = 0; \quad (2)$$

$$\frac{\partial}{\partial t} \left(\frac{1}{2} \rho U^2 + \frac{P}{\gamma - 1} + \frac{B^2}{2\mu_0} \right) + \nabla \cdot \left[\left(\frac{1}{2} \rho U^2 + \frac{\gamma}{\gamma - 1} P + \frac{B^2}{\mu_0} \right) \mathbf{U} - \frac{1}{\mu_0} \mathbf{U} \cdot \mathbf{B} \mathbf{B} \right] = 0; \quad (3)$$

$$\frac{\partial \mathbf{B}}{\partial t} + \nabla \cdot (\mathbf{U} \mathbf{B} - \mathbf{B} \mathbf{U}) = 0; \quad (4)$$

$$\nabla \cdot \mathbf{B} = 0, \quad (5)$$

where ρ , $\mathbf{U} = (U_x, U_y, U_z)$, P , $\mathbf{B} = (B_x, B_y, B_z)$, γ , and μ_0 denote, respectively, the mass density, flow velocity, pressure, magnetic field, the adiabatic index, and the permeability of free space.

Consider now the interaction and transmission of upstream fluctuations through an MHD shock governed by Equations (1)–(5). Let the shock fluctuate about a mean position $x=0$. We need to solve the time-dependent (non-conservation form of the) MHD Equations (1)–(5) on either side of the shock and then match the solutions across a free boundary (the shock). We therefore need to derive the free BCs. The shock surface and shock normal can be defined by

$$\Sigma: x - \phi(y, z, t) = 0, \quad \text{and} \\ \hat{\mathbf{n}} = \frac{(1, -\phi_y, -\phi_z, -\phi_t)}{\sqrt{1 + \phi_y^2 + \phi_z^2 + \phi_t^2}}, \quad (6)$$

respectively.

Recall the derivation of the Rankine–Hugoniot jump conditions (e.g., Chorin & Marsden 1990; Zank 2014) for a spacetime bounded region $S = S_1 \cup S_2$, where a discontinuity Σ with normal direction $\hat{\mathbf{n}}$ separates S_1 from S_2 . For a system of equations, $\mathbf{u}_t + \nabla \cdot (f(\mathbf{u})) = 0$, we let $\mathbf{F} = (f(\mathbf{u}), u)$ and define the spacetime divergence $\text{Div}(f_1, f_2) \equiv \nabla \cdot f_1 + \partial f_2 / \partial t$. On assuming a $C^\infty(\mathbf{x}, t)$ test function, it can then be shown that weak solutions must satisfy the BC $[\mathbf{F} \cdot \hat{\mathbf{n}}] = 0$ on Σ . By introducing $\text{Grad} \equiv (\nabla, \partial_t)$, expression (6) for $\hat{\mathbf{n}}$ immediately results. Since, e.g., the continuity Equation (1) can be expressed as $\text{Div} \mathbf{F}^\rho \equiv \text{Div}(\rho u_x, \rho u_y, \rho u_z, \rho) = 0$, it follows at once that $[\mathbf{F}^\rho \cdot \hat{\mathbf{n}}] = 0$ yields

$$-\phi_t[\rho] + [\rho u_x] - \phi_y[\rho u_y] - \phi_z[\rho u_z] = 0, \quad (7)$$

where henceforth $[Q] \equiv Q_2 - Q_1 = 0$ and the subscript 2 denotes downstream and 1 upstream. Similarly the remaining

conservation laws, Equations (2)–(5), yield the BCs

$$\begin{aligned}
& -\phi_t[\rho u_x] + \left[\rho u_x^2 + P + \frac{B^2}{2\mu_0} - \frac{B_x^2}{\mu_0} \right] \\
& - \phi_y \left[\rho u_x u_y - \frac{1}{\mu_0} B_x B_y \right] \\
& - \phi_z \left[\rho u_x u_z - \frac{1}{\mu_0} B_x B_z \right] = 0; \tag{8}
\end{aligned}$$

$$\begin{aligned}
& -\phi_t[\rho u_y] + \left[\rho u_x u_y - \frac{1}{\mu_0} B_x B_y \right] \\
& - \phi_y \left[\rho u_y^2 + P + \frac{B^2}{2\mu_0} - \frac{B_y^2}{\mu_0} \right] \\
& - \phi_z \left[\rho u_z u_y - \frac{1}{\mu_0} B_y B_z \right] = 0; \tag{9}
\end{aligned}$$

$$\begin{aligned}
& -\phi_t[\rho u_z] + \left[\rho u_x u_z - \frac{1}{\mu_0} B_x B_z \right] \\
& - \phi_y \left[\rho u_y u_z - \frac{1}{\mu_0} B_y B_z \right] \\
& - \phi_z \left[\rho u_z^2 + P + \frac{B^2}{2\mu_0} - \frac{B_z^2}{\mu_0} \right] = 0;
\end{aligned}$$

$$\begin{aligned}
& -\phi_t \left[\frac{1}{2} \rho u^2 + \frac{P}{\gamma - 1} + \frac{B^2}{2\mu_0} \right] \\
& + \left[\left(\frac{1}{2} u^2 + \frac{\gamma}{\gamma - 1} \frac{P}{\rho} + \frac{B^2}{\mu_0 \rho} \right) \right. \\
& \quad \left. (\rho u_x - \phi_y \rho u_y - \phi_z \rho u_z) \right. \\
& \quad \left. - \frac{1}{\mu_0} \mathbf{u} \cdot \mathbf{B} (B_x - \phi_y B_y - \phi_z B_z) \right] = 0; \tag{10}
\end{aligned}$$

$$\begin{aligned}
& \phi_t [B_x] + \phi_y [u_y B_x - u_x B_y] \\
& + \phi_z [u_z B_x - u_x B_z] = 0; \tag{11}
\end{aligned}$$

$$\begin{aligned}
& -\phi_t [B_y] + [u_x B_y - u_y B_x] \\
& - \phi_z [u_z B_y - u_y B_z] = 0; \tag{12}
\end{aligned}$$

$$\begin{aligned}
& -\phi_t [B_z] + [u_x B_z - u_z B_x] \\
& - \phi_y [u_y B_y - u_z B_z] = 0; \tag{13}
\end{aligned}$$

$$[B_x] - \phi_y [B_y] - \phi_z [B_z] = 0. \tag{14}$$

The BCs, Equations (7)–(14), are nine differential equations in the nine variables (ρ , \mathbf{u} , P , \mathbf{B} , and ϕ) that must be satisfied in transmitting an incident upstream fluctuation into the downstream region, i.e., the upstream (nonconservation) solutions of Equations (1)–(5) must be matched to the corresponding downstream solutions using Equations (7)–(14). The incident disturbances distort the shock surface, and the shape of the shock surface $\Sigma: x = \phi(y, z, t)$ is an unknown to be evaluated. This approach has been used to study the transmission of heliospheric turbulence across the heliopause into the very local interstellar medium (Zank et al. 2017b, 2019).

In identifying the upstream and downstream fluctuations, it is useful to use the nonconservation form of the momentum, energy, and induction equations

$$\begin{aligned}
\rho \left(\frac{\partial \mathbf{U}}{\partial t} + \mathbf{U} \cdot \nabla \mathbf{U} \right) &= -\nabla P \\
&+ \frac{1}{\mu_0} (\nabla \times \mathbf{B}) \times \mathbf{B}; \tag{15}
\end{aligned}$$

$$\frac{\partial P}{\partial t} + \mathbf{U} \cdot \nabla P + \gamma P \nabla \cdot \mathbf{U} = 0; \tag{16}$$

$$\frac{\partial \mathbf{B}}{\partial t} + \mathbf{U} \cdot \nabla \mathbf{B} = \mathbf{B} \cdot \nabla \mathbf{U} - \mathbf{B} (\nabla \cdot \mathbf{U}), \tag{17}$$

together with the entropy $S \propto \ln(P/\rho^\gamma)$ and vorticity $\boldsymbol{\xi} = \nabla \times \mathbf{U}$ equations,

$$\frac{\partial S}{\partial t} + \mathbf{U} \cdot \nabla S = 0; \tag{18}$$

$$\begin{aligned}
\frac{\partial \boldsymbol{\xi}}{\partial t} + \mathbf{U} \cdot \nabla \boldsymbol{\xi} - \boldsymbol{\xi} \cdot \nabla \mathbf{U} + \boldsymbol{\xi} (\nabla \cdot \mathbf{U}) \\
= \frac{1}{\rho^2} \nabla \rho \times \nabla (P - \mathbf{J} \times \mathbf{B}) \\
+ \frac{1}{\rho} (\mathbf{B} \cdot \nabla \mathbf{J} - \mathbf{J} \cdot \nabla \mathbf{B}). \tag{19}
\end{aligned}$$

In Equation (19), $\mu_0 \mathbf{J} = \nabla \times \mathbf{B}$ is the current.

Consider the case of an upstream weak mean magnetic field $\mathbf{B}_0 = B_0 \hat{\mathbf{z}}$ oriented perpendicularly to the flow vector $\mathbf{U}_0 = (U_x, U_y, \text{and } 0)$, such that transverse magnetic fluctuations (δB_x , δB_y , and 0) are of the same order of magnitude as B_0 and thus fluctuations $\delta B_z \ll B_0$. This may be interpreted as strong perpendicular magnetic turbulence despite the large plasma beta. Such an orientation yields magnetic islands in the plane of the flow velocity. This is illustrated schematically in Figure 2 and the weak mean magnetic field is in or out of the page, ensuring that the magnetic islands lie in the plane of the page. It follows that fluctuations δu_z can also be neglected. This is the same geometry used by Du et al. (2018) in simulating the interaction of 2D magnetic islands.

Since we assume 2D flows and $\mathbf{B}_0 = B_0 \hat{\mathbf{z}}$ constant, $\boldsymbol{\xi} \cdot \nabla \mathbf{U} = 0 = \mathbf{J} \cdot \nabla \mathbf{B}$ and $\mathbf{J} = (0, 0, J_z)$, $\boldsymbol{\xi} = (0, 0, \xi_z)$, and $\boldsymbol{\xi} \parallel \mathbf{J}$, which reduces Equation (19) to

$$\begin{aligned}
\frac{\partial \xi_z}{\partial t} + \mathbf{U} \cdot \nabla \xi_z + \xi_z (\nabla \cdot \mathbf{U}) \\
= \frac{1}{\rho^2} (\nabla \rho \times \nabla (P - \mathbf{J} \times \mathbf{B}))_z \\
+ \frac{1}{\rho} \mathbf{B} \cdot \nabla J_z. \tag{20}
\end{aligned}$$

Linearization of Equations (15)–(20), assuming $\mathbf{U} = \mathbf{U}_0 + (\delta u_x(x, y), \delta u_y(x, y), 0)$, $\mathbf{B} = \mathbf{B}_0 + (\delta B_x(x, y), \delta B_y(x, y), 0)$ (with $B_0 \sim O(\delta B_x, \delta B_y)$), $\rho = \rho_0 + \delta \rho$, and $P = P_0 + \delta p$, and seeking normal modes $\propto \delta \hat{\Psi} \exp i(\mathbf{k} \cdot \mathbf{x} - \omega t)$ yields the following propagating and advected modes:

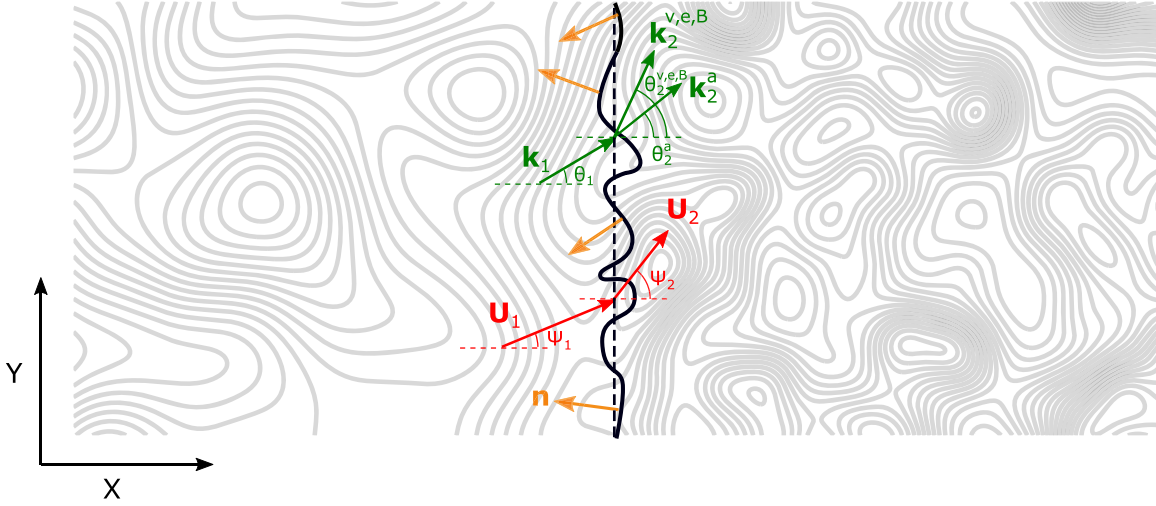


Figure 2. Cartoon showing a shock wave in the presence of magnetic flux ropes or islands upstream (1) and downstream (2) of the fluctuating shock front (black irregular curve). The upstream/downstream flow speed is denoted by $U_{1/2}$ and makes an angle $\Psi_{1/2}$ with the unperturbed shock normal. The wavevector \mathbf{k} is in the (x, y) plane with angle θ to the unperturbed shock normal. An incident mode with wavenumber k_1 impinges on the shock, distorting the shock front and modifying the shock normal direction $\hat{\mathbf{n}}$. We plot several shock normals $\hat{\mathbf{n}}$ at different shock locations, illustrating that the shock normal can assume different directions at different locations, and will furthermore change with time. Three gas dynamic modes (k_2^a , k_2^v , and k_2^B corresponding to acoustic, vorticity, and entropy modes) are emitted downstream for an incident gas dynamic mode. For an incident magnetic island, a magnetic island (k_2^B) is transmitted/generated downstream of the shock. The weak mean magnetic field $\mathbf{B}_0 = B_0 \hat{\mathbf{z}}$ is in/out of the page.

- (i) *Acoustic modes:* $\omega' = \pm a_0 k$, where $\omega' \equiv \omega - \mathbf{U}_0 \cdot \mathbf{k} \neq 0$, with eigenrelations

$$\begin{aligned} \delta \hat{\rho} &= \frac{\delta \hat{p}}{a_0^2}, \quad \delta \hat{\mathbf{u}} = \mp \frac{\mathbf{k}/k}{\rho_0 a_0} \delta \hat{p}, \\ \delta \hat{\mathbf{B}} &= 0, \quad a_0^2 = \frac{\gamma P_0}{\rho_0} \text{ (soundspeed)}. \end{aligned} \quad (21)$$

- (ii) *Entropy modes:* $\omega' = 0$ with eigenrelations

$$\begin{aligned} \delta \hat{s} &= -\frac{\gamma \delta \hat{p}}{\rho_0}, \quad \delta \hat{p} = 0, \\ \delta \hat{\mathbf{u}} &= 0, \quad \delta \hat{\mathbf{B}} = 0, \quad \delta \hat{p} \text{ arbitrary}. \end{aligned} \quad (22)$$

- (iii) *Vortical modes:* $\omega' = 0$, with eigenrelations, after introducing $\mathbf{k} = k(\cos \theta, \sin \theta) \equiv k(\alpha, \beta)$,

$$\begin{aligned} \delta \hat{p} &= 0, \quad \delta \hat{\mathbf{B}} = 0, \quad \delta \hat{\rho} = 0, \\ \delta \hat{\mathbf{u}} &\neq 0, \quad \delta \xi_z \neq 0; \\ \mathbf{k} \cdot \delta \hat{\mathbf{u}} &= 0 \implies \delta \hat{\mathbf{u}} = \delta \hat{\mathbf{u}}(-\beta, \alpha). \end{aligned} \quad (23)$$

- (iv) *Magnetic island modes:* $\omega' = 0$, with

$$\begin{aligned} \delta \hat{p} &= 0, \quad \delta \hat{\rho} = 0, \quad \delta \hat{\mathbf{u}} = 0, \\ \delta \hat{\mathbf{B}} &\neq 0, \quad \delta J_z \neq 0; \\ \mathbf{k} \cdot \delta \hat{\mathbf{B}} &= 0 \implies \delta \hat{\mathbf{B}} = \delta \hat{\mathbf{B}}(-\beta, \alpha). \end{aligned} \quad (24)$$

The dispersion equations and corresponding eigenrelations describe all possible compressible and incompressible fluctuations propagating in the high plasma beta region upstream and downstream of a shock for an assumed weak mean magnetic field orthogonal to the flow velocity. The acoustic modes correspond to the MHD fast modes in the limit of $V_A \ll a_0$ and the slow mode is automatically absent for propagation orthogonal to the mean magnetic field, i.e., because $u_z = 0$ and $B_z = 0$. The vortical and magnetic island modes correspond to Alfvén waves in the limit of $k_z = 0$. See the Lighthill analysis

presented in Zank et al. (2017a). The magnetic fluctuations decouple from the fluctuating velocity, density, and pressure. This approach specifically retains magnetic structures advected with the flow and Alfvénic fluctuations enter only at a higher order.

Consider now the interaction and transmission of vortical, entropy, acoustic, and magnetic island structures (i)–(iv) through a shock wave. Following the approach of McKenzie & Westphal (1968), we may consider the linearized transmission problem. Although the subscript “0” above refers to the mean flow upstream or downstream of the shock, it will in future be replaced by either “1” or “2” to indicate the upstream or downstream state. The mean perpendicular magnetic field does not enter the analysis being of the same order as the fluctuating magnetic field. Since the shock is perturbed by a spectrum of small amplitude linearized fluctuations $\delta \Psi \propto \exp i(\mathbf{k} \cdot \mathbf{x} - \omega t)$, we may assume that

$$\phi = \eta \exp i(\mathbf{k} \cdot (0, y, z) - \omega t), \quad (25)$$

where the amplitude η of the shock front distortion is $O(\epsilon)$. The $O(1)$ BCs that result from the linearization of Equations (7)–(14) yield the familiar jump conditions for the mean plasma variables

$$[\rho U_x] = 0; \quad (26)$$

$$[\rho U_x^2 + P] = 0; \quad (27)$$

$$[U_y] = 0; \quad (28)$$

$$\left[\frac{1}{2} U^2 + \frac{\gamma}{\gamma - 1} \frac{P}{\rho} \right] = 0, \quad (29)$$

which, in the high plasma beta limit, are simply the Rankine–Hugoniot conditions of gas dynamics. Although the following jump condition is derived formally at the next order,

$$[U_x B_0] = 0, \quad (30)$$

we include Equation (30) with Equations (26)–(29) because it describes the well-known change in the mean magnetic field \mathbf{B}_0

across a perpendicular shock, i.e., $U_{x1}/U_{x2} = B_{02}/B_{01} = r$, where r is the shock compression ratio. We remark that the transverse velocity component is unchanged across the shock, Equation (28), meaning that the leading order jump conditions can be transformed into a related inertial frame by moving into the transverse velocity frame. Such a transformation is discussed briefly in Appendix B.

The linearized higher-order jump conditions include the transverse magnetic field fluctuations, and can be expressed as

$$-\phi_t[\rho] + m \left[\frac{\delta\rho}{\rho} + \frac{\delta u_x}{U_x} \right] - \phi_y U_y[\rho] = 0; \quad (31)$$

$$\left[U_x \frac{\delta\rho}{\rho} + 2\delta u_x + \frac{\delta p}{\rho U_x} \right] = 0; \quad (32)$$

$$-\phi_t U_y[\rho] + m U_y \left[\frac{\delta\rho}{\rho} + \frac{\delta u_y}{U_y} + \frac{\delta u_x}{U_x} \right] - \phi_y[\rho U_y^2 + P] = 0; \quad (33)$$

$$-\phi_t \left[\frac{1}{2} \rho U^2 + \frac{P}{\gamma - 1} \right] + [\mathcal{E} \rho \delta u_x + m \mathbf{U} \cdot \delta \mathbf{u}] + m \left[\frac{1}{2} U^2 \frac{\delta\rho}{\rho} + \frac{a^2}{\gamma - 1} \frac{\delta p}{P} \right] - \phi_y U_y \mathcal{E}[\rho] = 0; \quad (34)$$

$$[U_x \delta B_y] = 0; \quad (35)$$

$$[\delta B_x] = 0, \quad (36)$$

where $m = \rho_1 U_{x1} = \rho_2 U_{x2}$, $a^2 = \gamma P / \rho$ is the (square of the) sound speed,

$$\mathcal{E} = \frac{1}{2} U_1^2 + \frac{a_1^2}{\gamma - 1} = \frac{1}{2} U_2^2 + \frac{a_2^2}{\gamma - 1},$$

and the subscripts 1(2) denote upstream(downstream) of the shock (Figure 2). The higher-order tangential momentum equation shows that $\phi_z = 0$, which is why it does not appear in Equations (31)–(36). Notice that in the perturbed BCs, Equations (31)–(36), the magnetic fluctuations are decoupled from the gas dynamic equations entirely, allowing Equations (35) and (36) to be solved separately.

The solution of the transmission problem requires solving for the fluctuating shock front, meaning that the perturbed shock front produces a perturbed shock normal across which the fluctuations are transmitted (Figure 2). The normal is determined by the gradient of the shock front equation $x = \phi(t, y, z)$ (Equation (6)). To obtain the perturbed fluctuations and the perturbed shock front equation/shock normal requires solving the higher-order Equations (31)–(36). Equations (31)–(36) are solved in the oblique flow velocity frame but can equally be solved in a different inertial frame, as pointed out by the referee. This can be accomplished by translating into a coordinate system moving transversely to the mean shock front at a velocity U_y , for example. On so doing, one obtains a system of equations equivalent to Equations (31)–(36), but without an incident oblique flow. For completeness, a brief derivation and equivalent system of equations is presented in Appendix B, and we have

verified that numerical solutions of both sets of equations yields the same results.

2.1. Transmission of Vortical Modes

We seek solutions $\delta\Psi = \delta\hat{\Psi} \exp i(\mathbf{k} \cdot \mathbf{x} - \omega t)$ and $\phi = \eta \exp i(k_y y - \omega t)$, where $\delta\Psi = (\delta\rho, \delta P, \delta\mathbf{u}, \text{ and } \delta\mathbf{B})$. Hence, $\phi_y = ik_y \phi$ and $\phi_t = -i\omega\phi$. We consider a vorticity mode advected in the upstream flow colliding with the shock and distorting the shock front. Three forms of gas dynamic fluctuations will diverge from the shock in the downstream region; an acoustic wave, an entropy mode, and a vortical mode, which, with the distorted shock amplitude, makes four unknown gas dynamic quantities. This corresponds to the four free BCs, Equations (31)–(34). From Equation (21), for the downstream acoustic modes, $\delta\hat{\rho}$ and $\delta\hat{\mathbf{u}}$ can be expressed through $\delta\hat{p}$. For the downstream entropy mode, from Equation (22), $\delta\hat{p} = 0$, $\delta\hat{\mathbf{u}} = 0$, and $\delta\hat{\rho}$ can be expressed through $\delta\hat{s}$. Finally, for the transmitted vorticity mode, Equation (23) shows that $\delta\hat{p} = \delta\hat{\rho} = \delta\hat{s} = 0$ and $\delta\hat{\mathbf{u}} \neq 0$. We may therefore rewrite all downstream variables $\delta\hat{\Psi}$ in terms of the diverging fluctuations, e.g.,

$$\begin{aligned} \delta\hat{\rho}_2 &= \delta\hat{\rho}_2^a + \delta\hat{\rho}_2^e + \delta\hat{\rho}_2^v \\ &= \delta\hat{\rho}_2^a + \delta\hat{\rho}_2^e = \frac{\delta\hat{p}_2}{a_2^2} - \frac{\rho_2}{\gamma} \delta\hat{s}_2; \end{aligned}$$

$$\begin{aligned} \delta\hat{\mathbf{u}}_{x2} &= \delta\hat{\mathbf{u}}_{x2}^a + \delta\hat{\mathbf{u}}_{x2}^v \\ &= \pm \frac{\cos\theta_2^a}{\rho_2 a_2} \delta\hat{p}_2 - \sin\theta_2^v \delta\hat{\mathbf{u}}_2, \end{aligned}$$

where $\delta\hat{\Psi}_2^{a,e,v}$ refer to the downstream fluctuating acoustic, entropy, and vorticity variables and $\theta_2^{a,e,v}$ to the downstream propagation direction of the acoustic, entropy, and vorticity modes.

To determine the downstream angles of propagation for the transmitted and generated modes resulting from an upstream vortical mode, we can assume that the frequency ω and tangential wavenumber k_y are continuous across the $O(1)$ shock, i.e., $\omega_1 = \omega_2 = \omega$ and $k_{y1} = k_{y2} = k_y$. Consider first the transmission/generation of a downstream vorticity/entropy mode from an incident vortical mode. Since $\omega'_1 = \omega_1 - U_{x1} k_{x1} - U_{y1} k_{y1} = 0$ and $\omega'_2 = \omega_2 - U_{x2} k_{x2} - U_{y2} k_{y2} = 0$, the continuity of ω , k_y , and U_y imply

$$\begin{aligned} \tan\theta_2^v &\equiv k_y/k_{x2} \\ &= \frac{U_{x2}}{U_{x1}} \tan\theta_1^v = r^{-1} \tan\theta_1^v, \end{aligned} \quad (37)$$

where θ_1^v is the angle made by the incident vorticity mode, $\psi_{1/2}$ the angle between the $O(1)$ shock normal and the upstream/downstream mean flow velocity, and $r \equiv \rho_2/\rho_1 = U_{x1}/U_{x2}$ is the shock compression ratio (see Appendix A). For the generation of a downstream acoustic mode, we need to solve

$\omega'_1 = 0$ and $\omega'_2 = \pm a_2 k_2$ simultaneously, which yields

$$\cot \theta_2^a = k_{x2}/k_y = -\frac{rM_{x2}^2}{1 - M_{x2}^2} \cot \theta_1^v \pm \frac{1}{\sqrt{1 - M_{x2}^2}} \left(\frac{r^2 M_{x2}^2}{1 - M_{x2}^2} \cot^2 \theta_1^v - 1 \right)^{1/2}, \quad (38)$$

where $M_{1/2} = U_{1/2}/a_{1/2}$. Evidently, two possible acoustic modes, forward/fast (+) and backward/slow (-), can be generated by an incident vortical mode. Notice that downstream acoustic modes generated by an incident vorticity mode with propagation angle θ_1 satisfying

$$\tan^2 \theta_1 \leq \frac{r^2 M_{x2}^2}{1 - M_{2x}^2}, \quad (39)$$

are either evanescent (and hence bounded since $\cot \theta_2^a = k_{x2}/k_y = a + ib$ implies a damping term $\propto -bk_y x$ and so ensures that the near field decays rapidly) or unbounded (and which are accordingly eliminated). The downstream acoustic wave field is therefore confined to propagation angles for which the discriminant in Equation (38) is ≥ 0 . Condition (39) can be relaxed slightly because for transmission, we require $k_x > 0$ and thus $\cot \theta_2^a > 0$. Hence, we need to choose the positive sign in Equation (38). To ensure $\cot \theta_2^a > 0$, the condition

$$\cot^2 \theta_1 > \frac{1}{r^2 M_{x2}^2} \text{ or } \tan^2 \theta_1 < r^2 M_{x2}^2, \quad (40)$$

must hold. Condition (40) is obviously a sufficient condition for condition (39).

On utilizing the above results, the linearized BCs to be solved for the distorted shock amplitude and the downstream acoustic, vorticity, and entropy amplitudes are given by

$$(r-1) \frac{\varpi - \overline{U_y k_y}}{M_1} X_1 - \cos \psi_1 X_2 - r \sin \theta_2^v X_3 + M_1 (M_2 \cos \psi_2 \pm \cos \theta_2^a) \sqrt{\frac{r}{P_2/P_1}} X_4 = -\sin \theta_1^v Y_3; \quad (41)$$

$$-X_2 - 2 \sec \psi_1 \sin \theta_2^v r X_3 + \left(\frac{M_1^2}{P_2/P_1} - 2M_1 \sqrt{\frac{r}{P_2/P_1}} \sec \psi_1 \cos \theta_2^a + r \sec^2 \psi_1 \right) X_4 = -2r \sec \psi_1 \sin \theta_1^v Y_3; \quad (42)$$

$$-\frac{k_y/k_0 \sec \psi_1}{\gamma M_1^2} (P_2/P_1 - 1) X_1 + \cos \theta_2^v X_3 \pm \sin \theta_2^a \frac{M_1}{\sqrt{r P_2/P_1}} X_4 = \cos \theta_1^v Y_3; \quad (43)$$

$$\begin{aligned} & \left((r-1) (\varpi - \overline{U_y k_y}) \left(\frac{1}{2} M_1^2 + \frac{1}{\gamma-1} \right) - \varpi \gamma^{-1} (P_2/P_1 - 1) \right) \frac{1}{M_1} X_1 \\ & - \frac{1}{2} \cos \psi_1 M_2^2 \frac{P_2/P_1}{r} X_2 \\ & + \left(M_1^2 \cos \psi_1 \sin \psi_1 \cos \theta_2^v - \left(r \left(\frac{1}{2} M_1^2 + \frac{1}{\gamma-1} \right) + \frac{M_1^2}{r} \cos^2 \psi_1 \right) \sin \theta_2^v \right) X_3 \\ & + \left(\frac{M_1^2}{r} \cos \psi_1 \left(\frac{1}{2} M_2^2 + \frac{\gamma}{\gamma-1} \right) \pm \frac{M_1}{\sqrt{r P_2/P_1}} \left(r \left(\frac{1}{2} M_1^2 + \frac{1}{\gamma-1} \right) + \frac{M_1^2}{r} \cos^2 \psi_1 \right) \cos \theta_2^a \right. \\ & \left. \pm \frac{M_1^3}{\sqrt{r P_2/P_1}} \cos \psi_1 \sin \psi_1 \sin \theta_2^a \right) X_4 \\ & = \left(M_1^2 \cos \psi_1 \sin \psi_1 \cos \theta_1^v - \left(\frac{1}{2} M_1^2 + \frac{1}{\gamma-1} + M_1^2 \cos^2 \psi_1 \right) \sin \theta_1^v \right) Y_3, \end{aligned} \quad (44)$$

where the normalized variables are defined as

$$X_1 = ik_0 \eta; \quad X_2 = \frac{\delta s_2}{\gamma}; \quad X_3 = \frac{\delta \hat{u}_2}{U_1}; \quad X_4 = \frac{\delta \hat{p}_2}{\rho_1 U_1^2}; \quad Y_3 = \frac{\delta \hat{u}_1}{U_1}, \quad (45)$$

$\varpi = \omega/\omega_0$, $\overline{U_y k_y} = U_y k_y/\omega_0 = U_1 k_y \sin \psi_1/\omega_0$, and a reference frequency ω_0 has been introduced. The \pm signs correspond to the choice in the acoustic dispersion relation $\omega' = \pm a_0 k$. Here, we choose the forward (+) acoustic mode. The mean downstream quantities (r , P_2/P_1 , ψ_2 , M_2) are determined from the solution of the mean Rankine–Hugoniot conditions, Equations (26)–(29), given in Appendix A. The mean upstream variables are prescribed, as is the upstream vorticity Y_3 .

Equations (41)–(44) form a linear system for specified values of the upstream Mach number M_{x1} , incident fluctuating amplitude Y_3 , and incident propagation angle θ_1^v , which is straightforwardly solved for the downstream wave field.

2.2. Transmission of Entropy Modes

The analysis for the transmission of advected upstream entropy modes follows that of the vorticity mode transmission problem described in Section 2.1 closely. The downstream vorticity and acoustic angles θ_2^v and θ_2^a are given by Equations (37) and (38), respectively. The left-hand side (LHS) of the linear system, Equations (41)–(44), is unchanged and the normalized right-hand side (RHS) source terms can be expressed as

$$\text{continuity:} \quad \text{RHS} = -\cos \psi_1 Y_2; \quad (46)$$

$$\text{normal momentum:} \quad \text{RHS} = -\frac{1}{r} Y_2; \quad (47)$$

$$\text{tangential momentum: } \text{RHS} = 0; \quad (48)$$

$$\text{energy: } \text{RHS} = -\frac{1}{2}M_1^2 \cos \psi_1 Y_2, \quad (49)$$

where $Y_2 = \delta \hat{s}_1 / \gamma$.

2.3. Transmission of Acoustic Modes

The transmission of an acoustic mode is a little more involved than described in Section 2.1 and the expressions for the downstream angles θ_2^v and θ_2^a are different. For θ_2^v , it is necessary to solve $\omega'_1 = \pm a_1 k$ and $\omega'_2 = 0$ to obtain

$$\cot \theta_2^v = k_{x2} / k_y = r \cot \theta_1^a \pm \frac{r}{M_{x1}} \csc \theta_1^a. \quad (50)$$

Solving $\omega'_1 = \pm a_1 k$ and $\omega'_2 = \pm a_2 k$ yields the downstream acoustic wave propagation angle

$$\cot \theta_2^a = \frac{a_1 M_{x1} \cot \theta_1^a \pm \csc \theta_1^a}{a_2 (1 - M_{x2}^2)} \times \left(-M_{x2} \pm \sqrt{1 - \frac{a_2^2}{a_1^2} \frac{1 - M_{x2}^2}{(M_{x1} \cot \theta_1^a \pm \csc \theta_1^a)^2}} \right). \quad (51)$$

A critical angle θ_{1c}^a is defined by the discriminant in Equation (51) being zero, i.e., when

$$\cot \theta_{1c}^a \pm \frac{1}{M_{x1} \sin \theta_{1c}^a} = \pm \frac{\sqrt{1 - M_{x2}^2}}{r M_{x2}}.$$

As discussed above, the waves generated downstream for upstream acoustic propagation angles yielding a negative discriminant are evanescent and exist only in the shock downstream near field.

As before, the LHS of the linear system, Equations (41)–(44), is unchanged and the normalized RHS source terms can be expressed as

$$\text{continuity: } \text{RHS} = M_1 (M_1 \cos \psi_1 \pm \cos \theta_1^a) Y_4; \quad (52)$$

$$\text{normal momentum: } \text{RHS} = r M_1 \left(M_1 \pm \cos \theta_1^a \csc \psi_1 + \frac{1}{M_1} \csc^2 \psi_1 \right) Y_4; \quad (53)$$

$$\text{tangential momentum: } \text{RHS} = \pm M_1 \sin \theta_1^a Y_4; \quad (54)$$

$$\begin{aligned} \text{energy: } \text{RHS} = & M_1 \left(\frac{1}{2} M_1^3 \cos \psi_1 \pm M_1^2 \right. \\ & \times \left(\frac{1}{2} \cos \theta_1^a + \cos^2 \psi_1 \cos \theta_1^a \right. \\ & \left. \left. + \cos \psi_1 \sin \psi_1 \sin \theta_1^a \right) \right. \\ & \left. + \frac{\gamma}{\gamma - 1} M_1 \cos \psi_1 \right. \\ & \left. + \frac{1}{\gamma - 1} \cos \theta_1^a \right) Y_4, \end{aligned} \quad (55)$$

where $Y_4 = \delta \hat{p}_1 / \rho_1 U_1^2$.

We will solve the acoustic wave transmission problem only, i.e., considering both forward (+ sign) and backward (-) acoustic modes, since the latter will be advected to the shock. For the present, we do not consider waves propagating from far downstream that collide with the back of the shock and which then results in a reflected acoustic mode and generated entropy and vortical modes.

2.4. Transmission of Upstream Magnetic Islands or Flux Ropes

Since the magnetic modes are fully decoupled from the gas dynamic fluctuations in the high plasma beta regime considered here, we solve Equations (35) and (36) directly. As before, since $\omega'_1 = 0$ and $\omega'_2 = 0$, we have

$$\tan \theta_2^B = k_y / k_{x2} = \frac{U_{x2}}{U_{x1}} \tan \theta_1^B, \quad (56)$$

where θ_1^B is the incident angle made by the magnetic islands as they are advected with the flow. Since $\delta \hat{\mathbf{B}} = \delta \hat{\mathbf{B}}(-\beta, \alpha)$, we obtain the downstream amplitude

$$\delta \hat{\mathbf{B}}_2 = r \frac{\cos \theta_1^B}{\cos \theta_2^B} \delta \hat{\mathbf{B}}_1 = \frac{\sin \theta_1^B}{\sin \theta_2^B} \delta \hat{\mathbf{B}}_1, \quad (57)$$

and $\delta \hat{\mathbf{B}}_2 = \delta \hat{\mathbf{B}}_2(-\beta_2, \alpha_2)$. Evidently, the amplification of magnetic islands by the shock in this plasma beta regime is modest, being at most a factor of the compression ratio r when the incident flow is normal to the shock, and is independent of shock obliquity.

3. Fluctuating Density, Kinetic, and Magnetic Energy Amplification and Spectra

Here, we illustrate solutions to the general set of linearized BCs, Equations (41)–(44), (46)–(49), and (52)–(55), for the fluctuating velocity, density, and magnetic field amplitudes. This includes computing the energies in the acoustic, vorticity, entropic, and magnetic island modes, i.e., we consider separate transmission problems for upstream vorticity, entropy, and acoustic fluctuations. The choice of the incident mean flow direction is irrelevant (see Appendix B). We assume plasma parameters roughly appropriate to 1 au with $M_{x1} = 3.75$, $n_1 = 10 \text{ cm}^{-3}$ for a shock compression ratio $r = 3.30$.

In Figure 3, we plot example solutions to the linearized BCs as a function of θ_1 , the angle made by the incident \mathbf{k} vector (see Figure 2) of a vorticity mode (Column 1), entropy mode (Column 2), forward (+) (Column 3), and backward (-) (Column 4) acoustic mode. The four downstream normalized variables η (X_1 , distorted fluctuating shock amplitude), $\delta \hat{s}_2$ (X_2 , fluctuating entropy amplitude), $\delta \hat{u}_2$ (X_3 , fluctuating vorticity velocity amplitude), and $\delta \hat{p}_2$ (X_4 , fluctuating acoustic pressure amplitude) are plotted as functions of θ_1 for each incident mode. The solid line depicts the real part and the dashed line the imaginary part of the solution. Complex solutions appear when the angle of the incident mode exceeds the critical angle defined by $\cot \theta^a$, changing from real to complex values. As discussed above, the pink region of θ_1 comprises only near-field modes that are evanescent, i.e., the region of complex solutions. The blue region identifies θ_1 values for which a downstream mode has a wavevector that is directed back toward the shock.⁵ For an incident vorticity mode (Column 1),

⁵ The blue region is related to the evolutionary conditions in that the requisite number of modes is transmitted/generated downstream but the corrugated shock front causes at least one of the modes to have a wavevector directed back toward to the mean shock front location. This is a perfectly valid realization and is not unphysical. If this were an advected mode, it would simply be carried away from the shock by the large-scale flow and would not interact again with the shock front. However, if it were an acoustic mode, then, depending on the phase velocity, it could in fact impinge on the shock from the downstream. This would then lead to the perturbation of the shock front, the reflection of the acoustic mode, and the generation of a vortical and entropy mode. As interesting as this problem is, we explicitly neglect wave interactions with the shock front from the downstream. As illustrated by the blue region, this is a very minor further effect and is therefore reasonable to neglect.

$$M_{x1} = 3.75, \overline{k_1 U_1} = 10$$

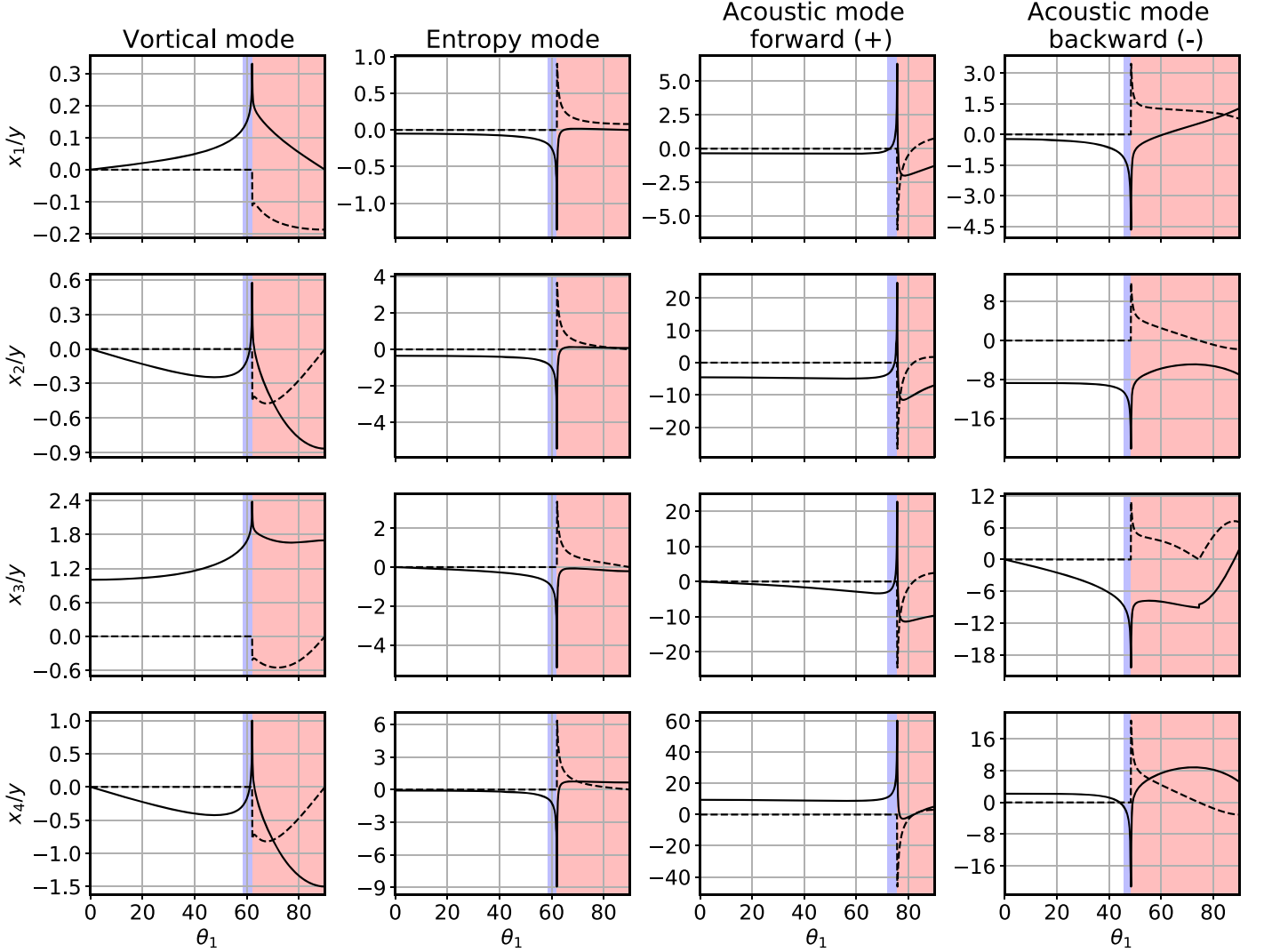


Figure 3. Solutions of the linearized BCs, Equations (41)–(44), (46)–(49), and (52)–(55), for a shock with compression ratio $r = 3.30$ as a function of θ_1 in the normalized variables $X_1/Y \propto \eta$, $X_2/Y \propto \delta\delta_2$, $X_3/Y \propto \delta\hat{u}_2$, and $X_4/Y \propto \delta\hat{p}_2$. Solid lines denote the real part of the complex solution and dashed lines the imaginary part. The columns correspond to the specific mode incident on the shock; Column 1—incident vortical mode, Column 2—entropy mode, Column 3—forward acoustic mode, Column 4—incident backward acoustic mode. The normalization Y corresponds to the Y_i , $i = 1, \dots, 4$, of the incident mode. See text for further discussion of the figure.

the amplitude of the shock front distortion increases with increasing θ_1 until θ_1^q . The incident vorticity mode generates an entropy mode with negative downstream amplitude $X_2 \propto \delta\delta_2$ that decreases with increasing θ_1 from zero until reaching a minimum, and then returns to zero and continues increasing in the blue region. The increasing amplification of the incident vorticity mode as a function of increasing θ_1 is illustrated in the third panel of Column 1 ($X_3/Y_1 = \delta\hat{u}_2/\delta\hat{u}_1$), showing that it peaks at θ_1^q . Finally, the normalized generated pressure fluctuation decreases from zero with increasing θ_1 until a minimum, and then increases back to zero at θ_1^q .

The transmission properties for the other incident modes are illustrated in the remaining three columns of Figure 3. The properties are self-explanatory and are examined in more detail when we discuss the respective variances below.

In Figure 4, we plot the variance of the individual (vorticity and acoustic) downstream velocity fluctuations and total kinetic energy as a function of the upstream or incident θ_1 of an

upstream vortical (Column 1), entropy (Column 2), and forward and backward acoustic (Columns 3 and 4) mode. The top row corresponds to the variance of the downstream vortical velocity $(\delta\hat{u}_2^v)^2$, the second row to the variance of the acoustic velocity $(\delta\hat{u}_2^a)^2$, and the third row to the total kinetic energy $\propto (\delta\hat{u}_2^v)^2 + (\delta\hat{u}_2^a)^2$. All these quantities are normalized to U_{x1}^2 . The variance is plotted only for $\theta_1 < \theta_1^q$ and up to the blue region of Figure 3. For an incident vorticity mode, the downstream kinetic energy is dominated by the amplified transmitted vortical mode, with the maximum transmitted energy being at $\theta_1 = \theta_1^q$ or peaking just before that. Very little energy resides in the acoustic modes. An incident entropy mode is very ineffective at generating downstream kinetic energy. By contrast, the largest kinetic energies are generated by an upstream acoustic mode, either forward or backward, colliding with the shock. For an incident forward acoustic mode, the downstream vortical variance is larger than that

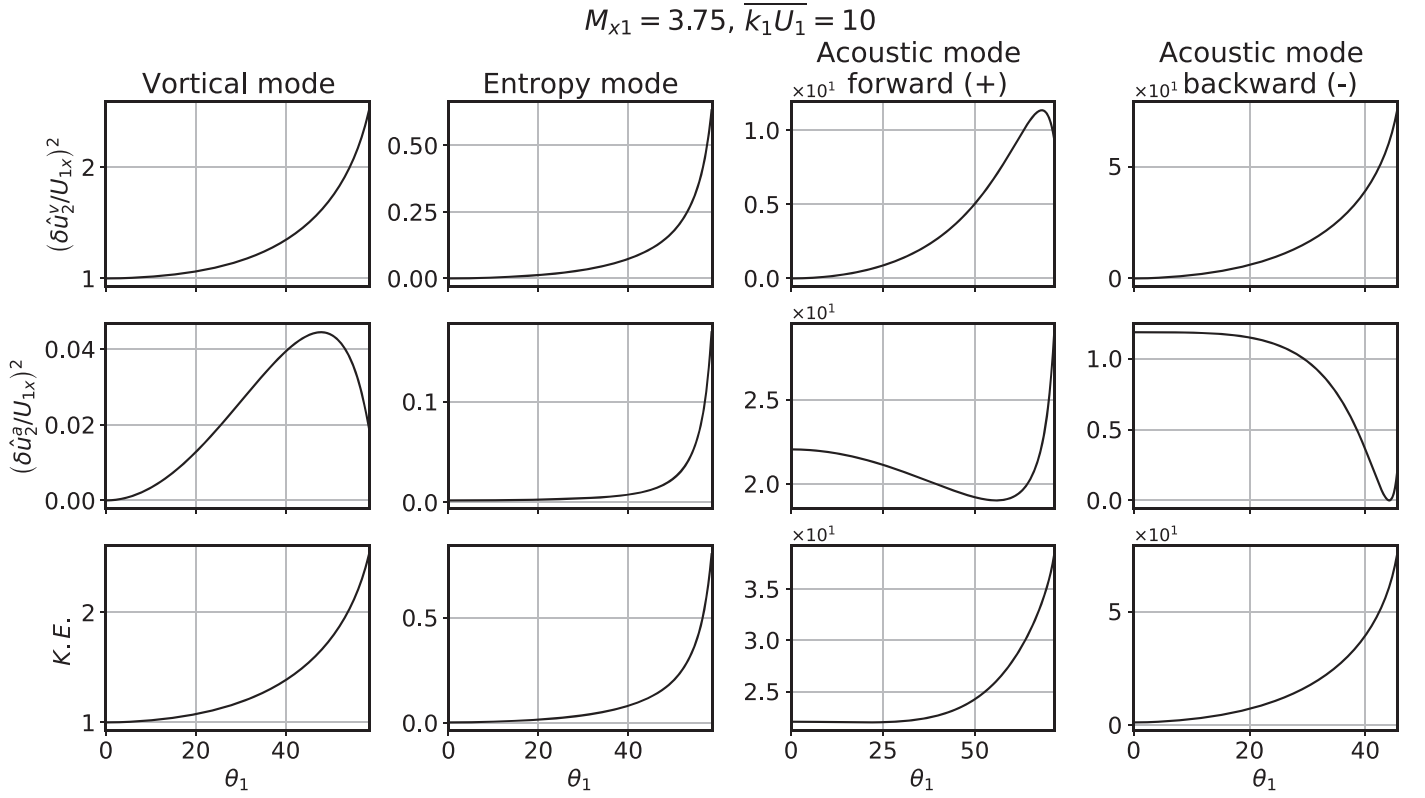


Figure 4. The variance or kinetic energy of the downstream fluctuating velocity field plotted as a function of the wavenumber of the incident fluctuation. Column 1 corresponds to an incident vortical mode, Column 2 to an incident entropy mode, and Columns 3 and 4 to an incident forward and backward (\pm) acoustic mode. The top row shows the variance of the downstream vortical velocity $(\delta \hat{u}_v^2)^2$, the second row the variance of the acoustic velocity $(\delta \hat{u}_a^2)^2$, and the third row the total kinetic energy $\propto (\delta \hat{u}_v^2)^2 + (\delta \hat{u}_a^2)^2$, all of which are normalized to U_{1x}^2 . See text for further discussion of the figure.

associated with an incident vortical mode. However, the variance of the downstream acoustic modes is more than 2 times larger than that of the downstream vortical variance for an incident forward acoustic mode. For an incident backward acoustic mode, the generated vortical variance can be from one to two orders of magnitude larger than the amplified downstream acoustic variance.

Figure 5 is a plot of the fluctuating density variance in a similar format as Figure 4. The downstream density fluctuations comprise contributions from the entropy and acoustic mode. All these quantities are normalized to ρ_1 . For an incident vortical mode, the downstream density variance is dominated by the density associated with the acoustic mode. There is more amplification of the density variance in the case of an incident entropy mode, at least compared to an incident vortical mode. For the incident forward acoustic mode, the transmitted acoustic density variance is larger than the entropy density variance by about a factor of ~ 3 . For an incident backward acoustic mode, the reverse is true with the entropy variance being larger by nearly two orders of magnitude for some angles of incidence.

In Figure 6, we plot the variance of the downstream fluctuating magnetic field $\delta \hat{B}_2^2$ as a function of θ_1^B for an incident magnetic field fluctuation. As seen in Equation (57), the downstream variance depends on r , and there is no cutoff angle for transmission. The amplification decreases from ~ 10 to 1 for increasing θ_1^B .

Before turning to the transmission of upstream spectra, we note that the downstream wavenumber k_{x2} depends on both the

mode incident on the shock, the upstream wavenumber k_{x1} (or equivalently θ_1), and the downstream transmitted/excited mode. As a consequence, the maximum wavenumber can be different for each of the excited/transmitted downstream states. This is illustrated in Figure 7, which shows the change in the transmitted and generated downstream wavenumber k_2/k_1 for an incident magnetic island, vortical, or forward/backward acoustic mode. The wavenumber behavior for an incident (and transmitted/generated) entropy mode is the same as the vorticity mode case. The downstream wavenumber is plotted as a function of the incident wave mode θ_1 and it is evident that the vortical and entropy mode downstream wavenumber k_2 is larger than the acoustic wavenumber k_2 . Each of the k_2 values is plotted for θ_1 less than or equal to the respective cutoff values at which the downstream solution becomes damped and exists only in the near field. As we show in the set of spectral figures below, Figure 7 implies that the high k part of the downstream variance spectrum would be dominated by vortical (in kinetic energy) and entropy (in density variance) modes.

The next set of figures illustrates the transmission of an upstream spectrum of vortical (Figure 8), entropy (Figure 9), forward acoustic (Figure 10), backward acoustic (Figure 11), and magnetic island (Figure 12) fluctuations. For each of the cases, the orange curve corresponds to the assumed upstream isotropic power spectrum of the variance of the incident mode $k = |\mathbf{k}|$, with the form (e.g., Zank 2014)

$$E(k) \propto (\delta X_i)^2 k \propto \frac{1}{1 + (k\ell)^\nu}, \quad (58)$$

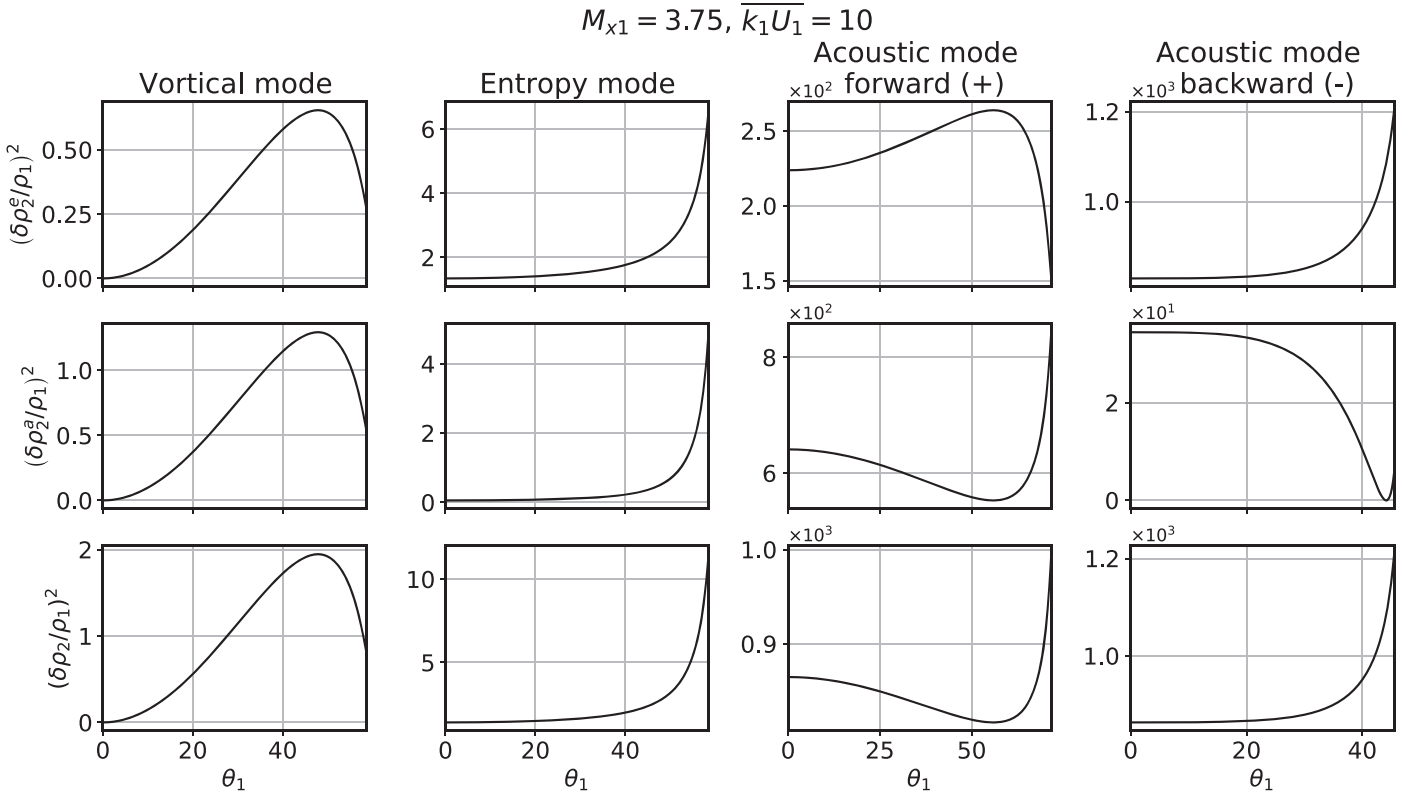


Figure 5. The variance of the downstream fluctuating density plotted as a function of θ_1 of the incident fluctuation. The columns have the same format as Figure 4. The top row shows the variance of the downstream density associated with the entropy mode $(\delta\rho_2^e)^2$, the second row the variance of the acoustic density $(\delta\rho_2^a)^2$, and the third row the variance of the total fluctuating density $\propto(\delta\rho_2^e)^2 + (\delta\rho_2^a)^2$, all of which are normalized to ρ_1^2 .

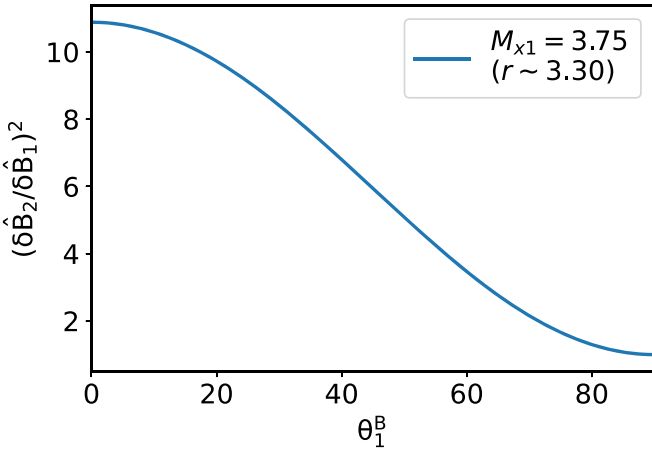


Figure 6. Variance of the downstream fluctuating magnetic field $\delta\hat{B}_2^2$ as a function of the incident magnetic field fluctuation wavenumber angle θ_1^B for a shock with compression ratio $r = 3.30$.

where $(\delta X_i)^2 \propto (\delta u^\nu)^2$, etc., ℓ is the correlation length/bend-over scale, and ν is the power-law index, here taken typically to be $5/3$. Thus, we consider the transmission of fluctuations in both the energy-containing and inertial ranges. The downstream spectrum is calculated as follows: (1) For the upstream spectrum, we prepare a number of waves assuming an omnidirectional power spectrum with θ_1 randomly distributed from 0 to $\pi/2$; (2) we calculate θ_2 and the amplitudes for each of the vortical, entropy, and acoustic modes transmitted or generated downstream for each incident wave using the LHS of the linear

system, Equations (41)–(44), with the appropriate source terms, and (3) we calculate the power spectrum of the downstream waves in k - θ_2 space for each of the generated modes and then integrate over θ_2 to obtain the downstream omnidirectional power spectrum. A similar procedure is followed in calculating the transmission of an upstream magnetic field spectrum.

Figure 8 shows the transmission of an upstream spectrum of vortical modes for a shock with compression ratio $r = 3.30$. The top panels show the downstream kinetic energy spectrum for the transmitted vortical modes (left panel), the generated acoustic modes (middle), and the total kinetic energy (right). The orange spectrum depicts the assumed upstream spectrum. The downstream spectrum is dominated by the transmitted vorticity fluctuations, the spectral amplitude in downstream acoustic modes being two orders of magnitude smaller. The spectral amplification of the upstream vortical fluctuations is about a factor of 2.5 in the energy-containing range and ~ 10 in the inertial range. Since the turbulence-shock transmission problem is linear, the spectral shape is preserved, although the downstream correlation length/bendover scale is smaller than the upstream value. The maximum downstream value of k is ~ 3 times larger than the prescribed upstream maximum value for downstream vortical fluctuations, but is approximately the same for the downstream generated acoustical modes, as discussed above. This leads to an almost imperceptible step in the downstream total kinetic energy spectrum at high k values, which in principle could lead to a slightly steeper spectrum were one to fit a single power law to the inertial range. However, the inertial range slopes of the downstream vortical, acoustic, and total kinetic energy spectra are essentially $-5/3$ and the same as the upstream spectra.

$$M_{x1} = 3.75 \text{ (} r \sim 3.30 \text{)}$$

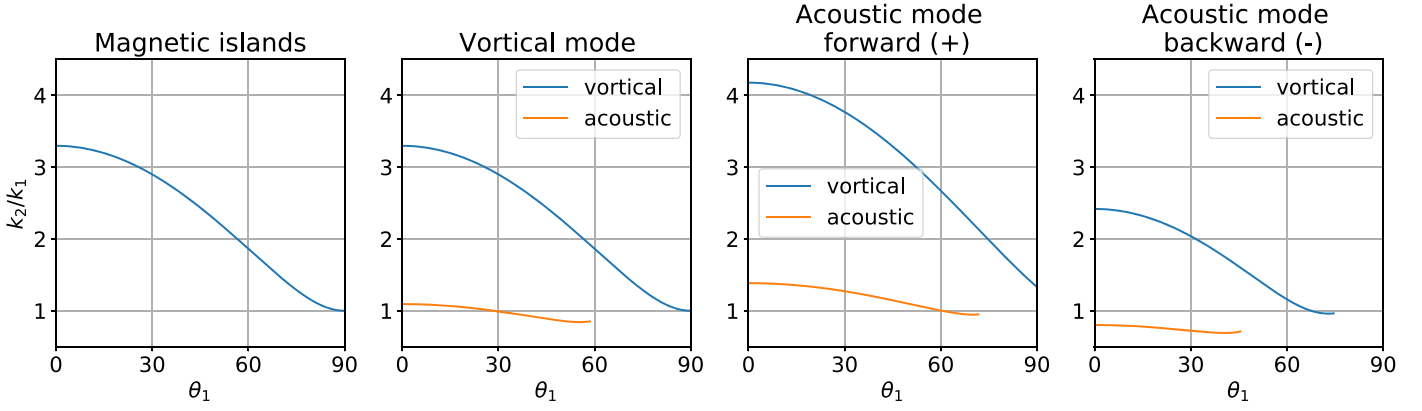


Figure 7. Plot of the downstream magnetic island, vortical, entropy, and acoustic wavenumbers k_2 relative to the wavenumber k_1 for an incident magnetic island, vortical, entropy, forward, and backward acoustic mode as a function of the incident propagation angle θ_1 .

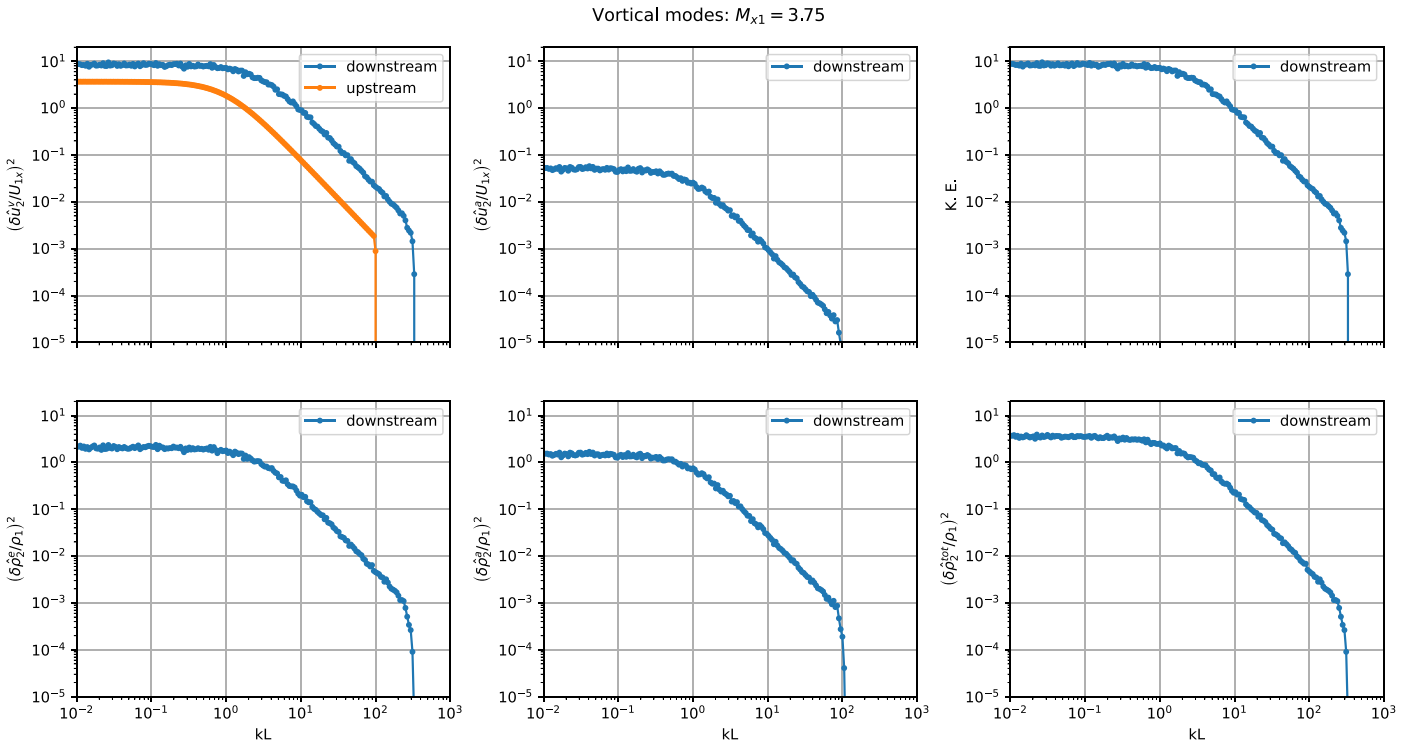


Figure 8. Downstream spectra generated by upstream vortical fluctuations (orange curve). The top row shows the spectra for the downstream vortical, acoustic, and total kinetic energy, and the lower panel shows spectra for the downstream entropy, acoustic, and total density variance.

The bottom row shows the generated downstream entropy and acoustic density variance spectra. The density spectrum associated with the entropy closely resembles the shape of the vortical spectrum. The amplitudes of the downstream entropy and acoustic spectra are similar within a factor of ~ 2 . The density variance spectra are $k^{-5/3}$ in the inertial range, and the total density variance spectrum exhibits a very small step for the same reason as before.

Corresponding to the results of Figure 8, Figure 9 shows downstream spectra for an incident spectrum of upstream entropy fluctuations. In this case, it is vortical and acoustic modes that are generated downstream along with the transmitted entropy modes. The entropy modes are amplified on transmission downstream, by about a factor 2 in the energy-containing range and by ~ 10 in the inertial range. The

downstream generated kinetic energy is dominated by the incompressible vortical fluctuations rather than the acoustic modes and the inertial range exhibits a $k^{-5/3}$ power law for both the downstream vortical and acoustic variances.

Illustrated in Figure 10 are the downstream velocity and density variance spectra transmitted and generated by an upstream isotropic spectrum of forward propagating acoustic modes. In this case, both upstream velocity and density fluctuations perturb the shock. The incident acoustic velocity variance is amplified significantly, by a factor of ~ 11 and ~ 12.5 in the energy-containing and inertial ranges. The correlation length/bendover scale for the downstream acoustic fluctuations is similar to that upstream. The spectral amplitude of the vorticity kinetic energy variance is about a factor of 2 less than that of the acoustic variance, and it exceeds the

Entropy modes: $M_{x1} = 3.75$

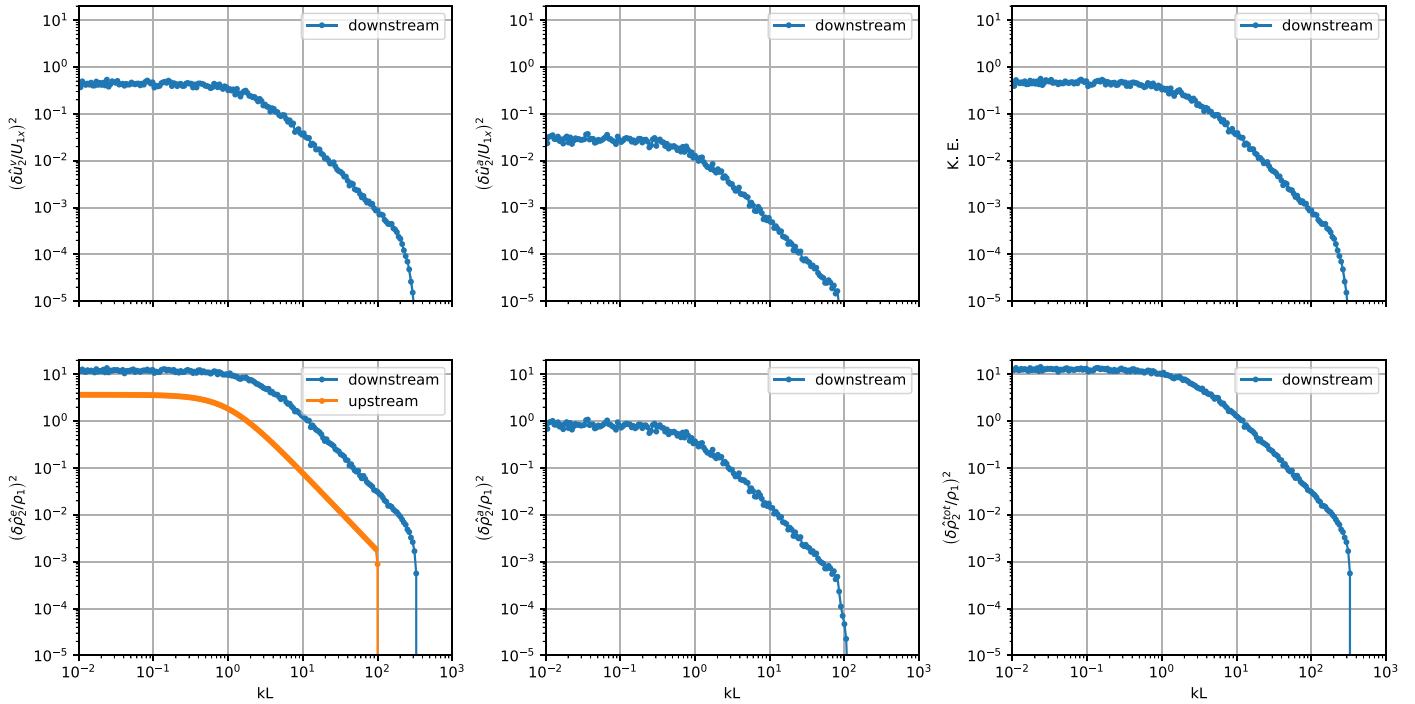


Figure 9. In the same format as Figure 8, spectra for an incident spectrum of upstream entropic fluctuations (orange curve).

Acoustic modes (forward): $M_{x1} = 3.75$

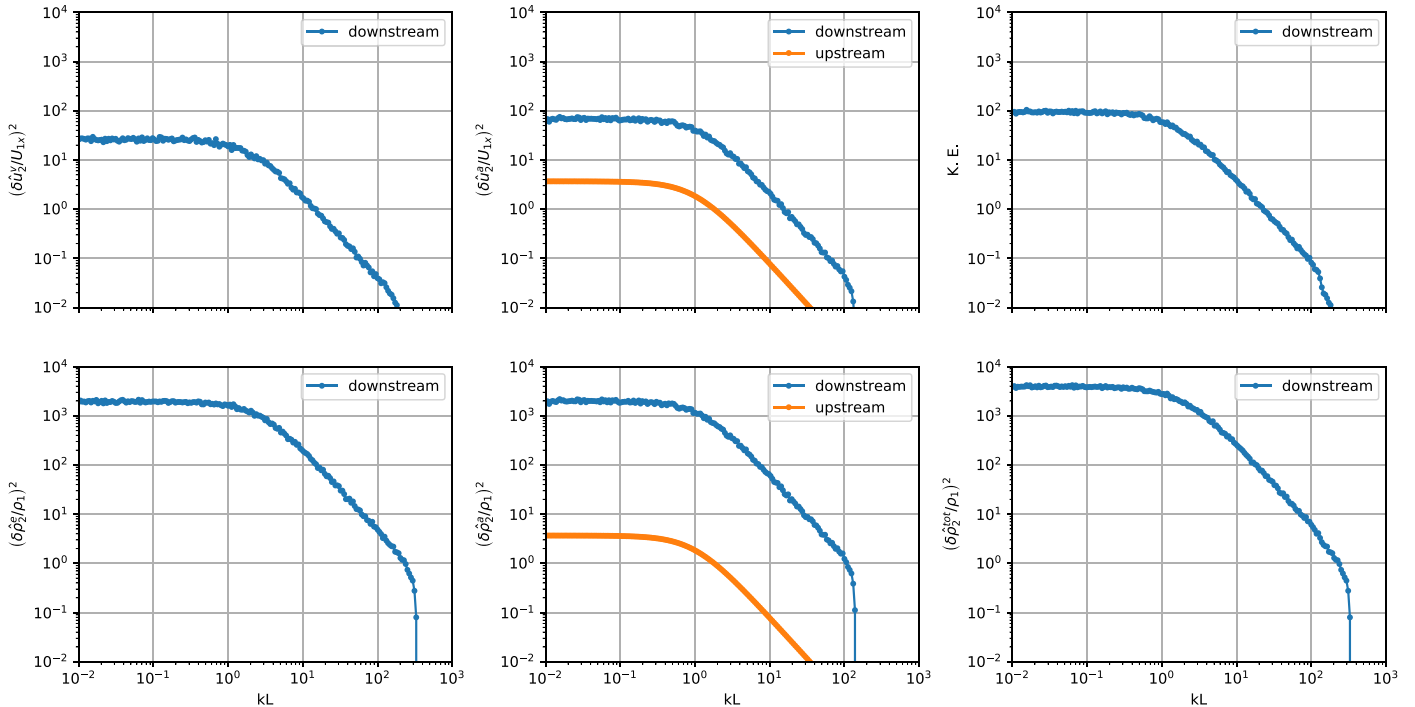


Figure 10. In the same format as Figure 8, spectra for an incident spectrum of upstream forward propagating acoustic velocity and density fluctuations (orange curves).

prescribed upstream acoustic kinetic energy. The maximum downstream vortical wavenumber is about 3 times larger than the maximum upstream acoustic wavenumber and larger by at least 2 than the maximum downstream acoustic wavenumber. Consequently, the total downstream kinetic energy spectrum exhibits a clear double power-law structure separated by a step.

Fitting a simple power law to the inertial range of the total kinetic energy spectrum would therefore yield a spectrum that appears to be steeper than that upstream. Finally, the downstream density variance spectra for the generated entropic and transmitted acoustic fluctuations are almost identical. The maximum wavenumber for the entropy fluctuations exceeds

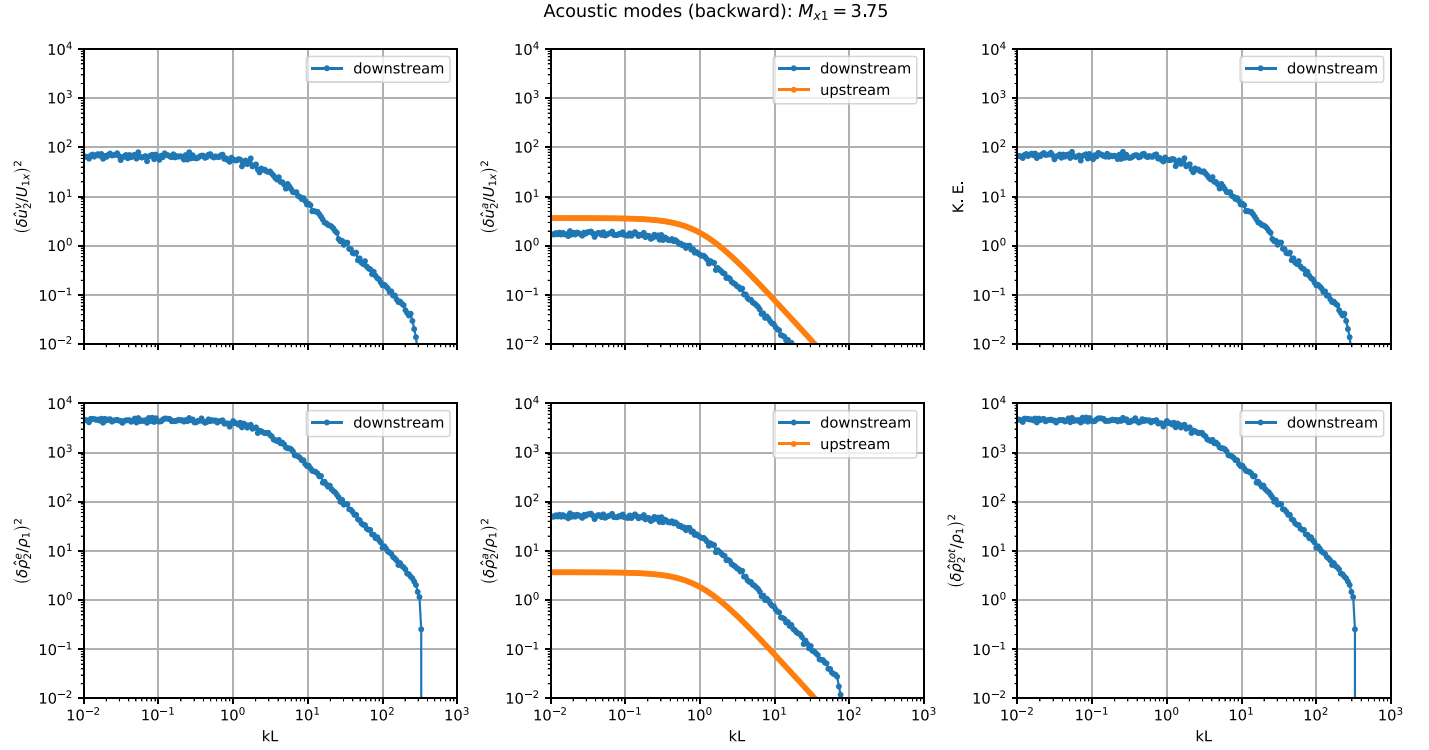


Figure 11. In the same format as Figure 8, spectra for an incident spectrum of upstream backward propagating acoustic velocity and density fluctuations (orange curves).

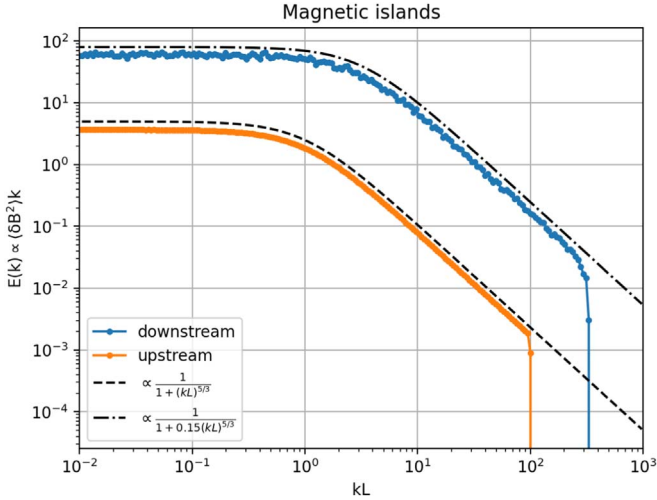


Figure 12. Downstream spectrum for incident upstream magnetic island fluctuations (orange spectrum) transmitted across a shock with compression ratio 3.30.

that of the acoustic fluctuations. As a result, the high wavenumber part of the density variance spectrum exhibits a small step followed by a power law.

An incident spectrum of upstream backward propagating acoustic fluctuations yields downstream spectra that are substantially different than those derived from forward propagating acoustic fluctuations, as illustrated in Figure 11. The transmitted acoustic kinetic energy spectrum is depressed compared to the upstream spectrum. However, the kinetic energy in downstream vortical modes dominates the total kinetic energy, exceeding the acoustic kinetic energy by a factor of ~ 40 in the energy-containing range and ~ 400 in the inertial ranges, respectively. The downstream density variance is dominated by

the excited entropy modes and not the acoustic modes, being larger in the energy-containing range by nearly two orders of magnitude and nearly three orders in the inertial range.

Consider now the downstream spectral variance of a spectrum of transmitted upstream fluctuating magnetic islands, as shown in Figure 12. The downstream correlation length is decreased. The magnetic island variance spectrum increases 16-fold over the upstream spectrum in the energy-containing range and ~ 100 times in the inertial range, implying a significant increase of magnetic energy density downstream of the shock. The transmitted downstream spectrum closely resembles the form of the upstream spectrum—the correlation length/bendover scale decreases downstream and the maximum downstream wavenumber is about 3 times larger than the maximum upstream wavenumber. The spectral characteristics are independent of shock obliquity.

It is of interest to combine the gas dynamic and magnetic field quantities in terms of the Elsässer variables in order to determine the relative changes of the kinetic and magnetic energy and the relative flux of total energy (Zank et al. 2017a). Borovsky (2020) discusses the effect of interplanetary shocks on the Alfvén ratio and the cross helicity (also called the Alfvénicity). Here, we use the results above to derive the normalized residual energy associated with fluctuations $\delta\sigma_r \equiv \delta\mathcal{E}_r / \delta\mathcal{E}_T$, the fluctuation normalized cross helicity $\delta\sigma_c \equiv \delta\mathcal{E}_c / \delta\mathcal{E}_T$, the fluctuation Alfvén ratio $\delta r_A \equiv (\delta u)^2 / ((\delta B)^2 / \mu_0 \rho)$, and the compressibility $C \equiv (\delta u^a)^2 / ((\delta u^v)^2 + (\delta B)^2 / (\mu_0 \rho))$, where (Zank et al. 2018)

$$\begin{aligned} \delta\mathcal{E}_T &= (\delta u)^2 + \frac{(\delta B)^2}{\mu_0 \rho}; & \delta\mathcal{E}_r &= (\delta u)^2 - \frac{(\delta B)^2}{\mu_0 \rho}; \\ \delta\mathcal{E}_c &= 2\delta\mathbf{u} \cdot \frac{\delta\mathbf{B}}{\sqrt{\mu_0 \rho}}. \end{aligned} \quad (59)$$

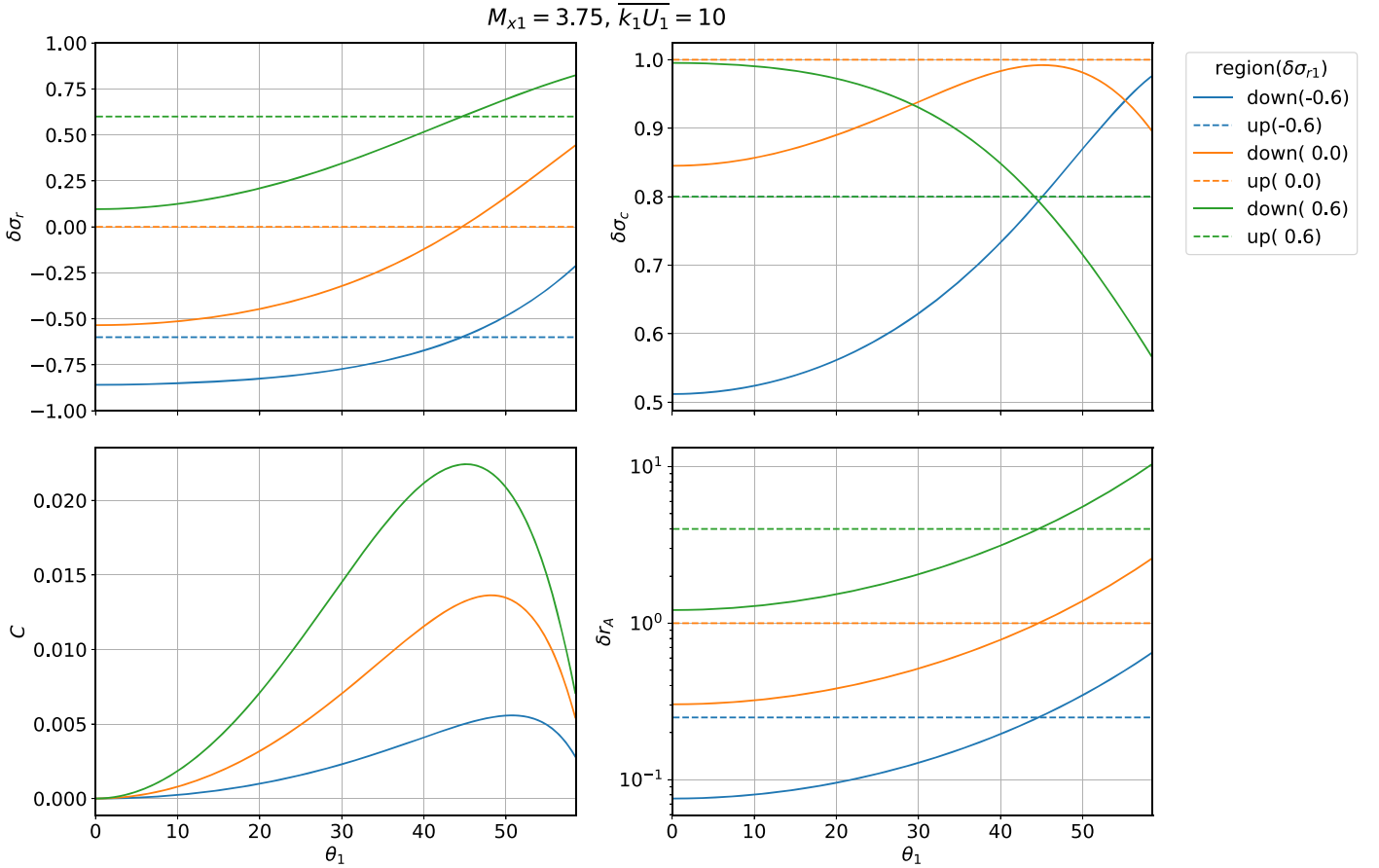


Figure 13. Clockwise from top left: downstream fluctuating residual energy $\delta\sigma_r$, cross helicity $\delta\sigma_c$, Alfvén ratio δr_A , and compressibility C as functions of θ_1 . The color coding refers to the choice of the value of the upstream $\delta\sigma_{r1}$: (blue) $\delta\sigma_{r1} = -0.6$, (orange) $\delta\sigma_{r1} = 0$, and (green) $\delta\sigma_{r1} = 0.6$. The dashed line refers to upstream and the solid line to the downstream values.

We do not exhaustively discuss the results as we did above but restrict attention to the single case of incident vortical and magnetic island fluctuations. We assume three possible combined gas dynamical-magnetic island upstream states based on the normalized residual energy (i.e., the net balance in magnetic and kinetic energy density): (1) $-1 < \delta\sigma_r < 0$; (2) $\delta\sigma_r = 0$, and (3) $0 < \delta\sigma_r < 1$. Illustrated in the four panels of Figure 13 are in clockwise order the residual energy, cross helicity, Alfvén ratio, and compressibility as functions of θ_1 . The dashed constant value lines correspond to the upstream state and the solid lines to the downstream value as a function of the upstream mode propagation angle θ_1 . The $\delta\sigma_r$ plots show that in all cases, regardless of the upstream value of $\delta\sigma_{r1}$, $\delta\sigma_{r2} < \delta\sigma_{r1}$ for $\theta_1 < 40^\circ$, indicating that for these θ_1 the downstream magnetic energy increased more relative to the increase in kinetic energy compared to the upstream residual energy. For angles greater than 40° , the kinetic energy downstream increased more relative to the increase in magnetic energy. The downstream cross helicity changes quite significantly across the shock, as illustrated in the top right panel of Figure 13. With the exception of the upstream $\delta\sigma_{r1} > 0$ case, the cross helicity decreases across the shock for $\theta_1 < 40^\circ$, and for $\delta\sigma_{r1} = 0$, it remains less than $\delta\sigma_{c1}$. By contrast, for the $\delta\sigma_{r1} > 0$ case, $\delta\sigma_{c2} > \delta\sigma_{c1}$ for $\theta_1 < 40^\circ$. The downstream fluctuating Alfvén ratio $\delta r_{A2} < \delta r_{A1}$ for all $\theta_1 < 40^\circ$, monotonically increases with increasing θ_1 . Finally, the compressibility C is 0 upstream but

increases, peaks, and then decreases for all upstream choices of $\delta\sigma_{r1}$.

In closing this systematic study of the transmission properties of an upstream turbulent spectrum of fluctuations across a shock, we show in Figure 14 the transmission of an incident vortical spectrum for a weak shock (top two rows, compression ratio $r = 1.5$) and a strong shock (bottom two rows, compression ratio $r = 3.9$). Other than the differences in amplification from the prior case ($r = 3.30$), the characteristics of the downstream transmitted and generated spectra are very similar. In the weak shock case, notice that a step in the density variance spectrum (due to smaller k range of acoustic waves) discussed earlier is now clearly visible. Similar comments apply to the cases of other incident wave mode spectra.

4. Comparison of Theory and Observations

Although the theory presented in Section 2 is of necessity somewhat idealized, we consider here its application to three shocks. Figure 15 shows the magnetic field, flow velocity, and proton density in the vicinity of shock crossing events observed at radial distances of 1, 5, and 84 au. The last two shock events were studied in detail by Zhao et al. (2019a) and Zhao et al. (2019b) in the context of magnetic flux ropes that were identified upstream and downstream of the shock. The shock parameters, including the shock location and shock compression ratio, which is determined by the ratio of the downstream and upstream density, and sonic Mach number in the shock rest

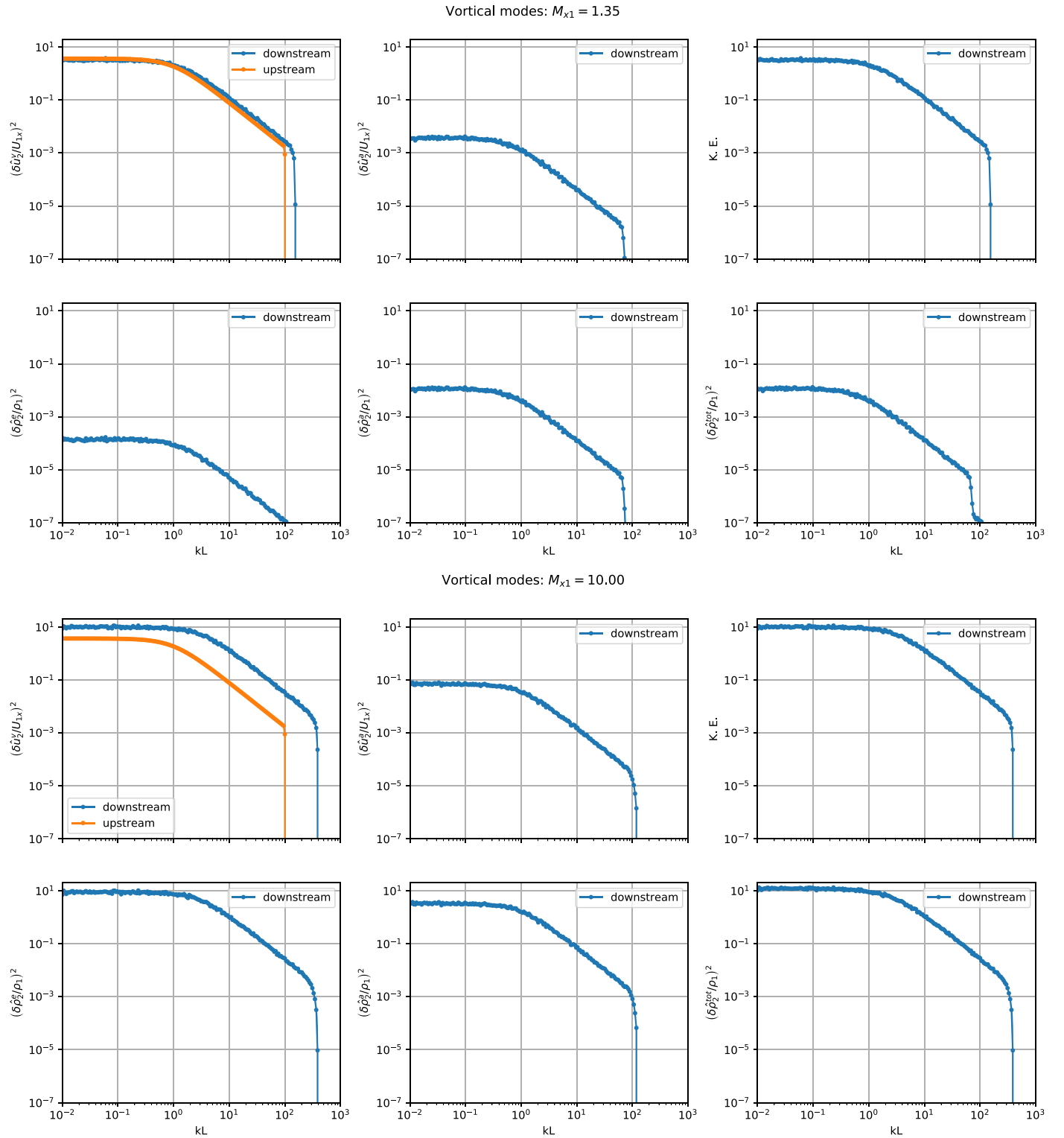


Figure 14. In the same format as Figure 8, spectra for an incident spectrum of upstream vortical fluctuations (orange curve) for a weak shock (top two rows, $r = 1.5$) and strong shock (bottom two rows, $r = 3.9$).

frame, are summarized in Table 1. The Mach number is derived from the Rankine–Hugoniot conditions after assuming the observed shock compression ratio. The HTS compression ratio is assumed to be 2.73 based on the analysis of Zank et al. (2018).

To determine the applicability of the general theory, we examined the assumption of the relative strength of the

fluctuating magnetic field to the upstream mean magnetic field, finding that for the (1) Wind event: $\delta B/B_0 = 0.54$ and $\delta B_{\perp}/B_0 = 0.5$; (2) Ulysses event: $\delta B/B_0 = 0.68$ and $\delta B_{\perp}/B_0 = 0.59$, and (3) Voyager 2 event: $\delta B/B_0 = 12.47$ and $\delta B_{\perp}/B_0 = 10$. As we discuss below, these were determined from 2 hr, 3 hr, and 455 day averages upstream of the shock. The large $\delta B/B_0$ in the upstream Voyager 2 event could be due to shocks

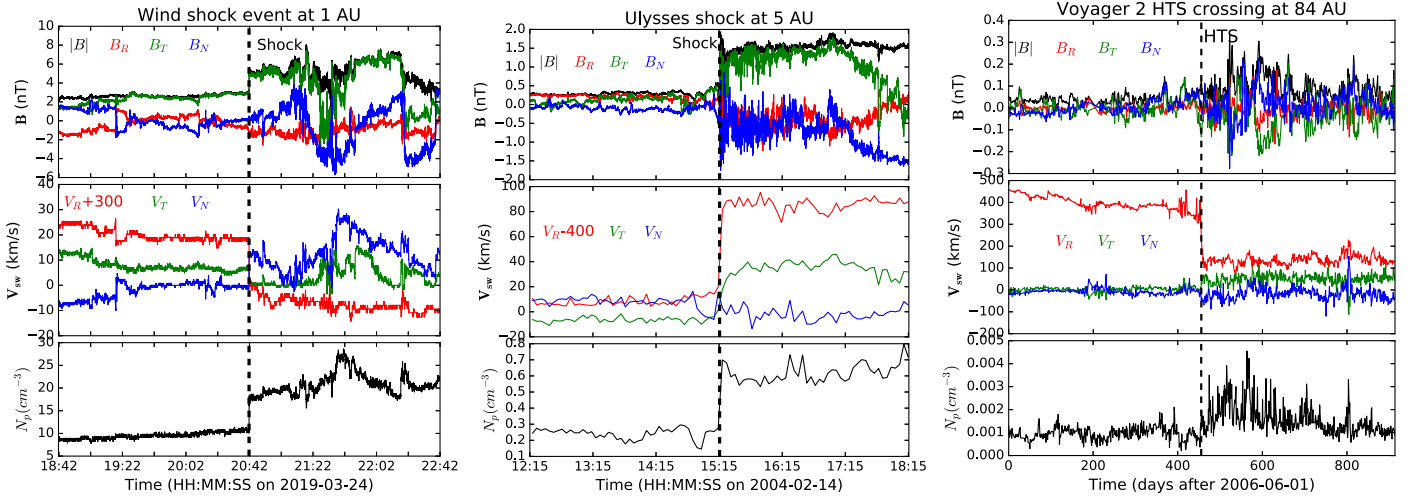


Figure 15. In situ observations of three shock events at different heliocentric distances. From left to right, the panels show Wind, Ulysses, and Voyager 2 measurements of magnetic field, solar wind speed, and proton density at 1, 5, and 84 au, respectively. The vertical dashed line in each panel shows the arrival time of the shock.

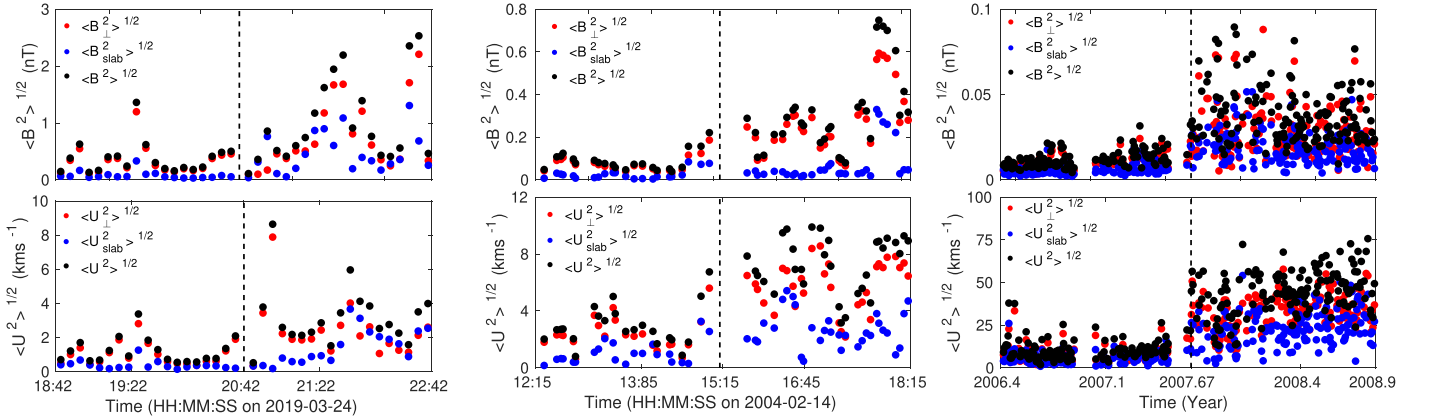


Figure 16. Plot of the fluctuating magnetic field variances (top panels) and fluctuating velocity field variances upstream and downstream of the shock observed by (left) Wind, (middle) Ulysses, and (right) Voyager 2. The variances correspond to the fluctuating 2D magnetic field components $\langle \delta B_{2D}^2 \rangle$, the slab variance $\langle \delta B_{\text{slab}}^2 \rangle$, and the total fluctuating magnetic field variance $\langle \delta B^2 \rangle$. By utilizing the magnetic field coordinate system, the fluctuating velocity field can be decomposed similarly into $\langle \delta u_{2D}^2 \rangle$, $\langle \delta u_{\text{slab}}^2 \rangle$, and $\langle \delta B^2 \rangle$.

Table 1

Shock Parameters Used to Evaluate the Downstream Magnetic Field, Kinetic Energy, and Density Variance Spectra for the Wind, Ulysses, and Voyager 2 Shock Events

	Position [au]	Mach Number M_{s1}	Compression Ratio
Wind	1	1.9	2.22
Ulysses	5	2.29	2.55
Voyager 2	84	1.79	2.73

in the upstream region. The velocity profile upstream of the HTS exhibits numerous spikes. However, downstream of the HTS, the ratios are much smaller with $\delta B/B_0 \sim 2.8$ and $\delta B_{\perp}/B_0 \sim 2$. The derived values of the ratio $\delta B/B_0$ suggest that $B_0 \sim O(\delta B)$ is a reasonable assumption for these three events, and moreover, the values of the ratio $\delta B_{\perp}/B_0$ indicate that most of the power indeed resides in the 2D magnetic field fluctuations. This is seen more clearly in Figure 16, in which the upstream and downstream 2D, slab, and total variance in

the fluctuating magnetic field and, in the same coordinates, the corresponding 2D, slab, and total variance in the fluctuating velocity field are computed.⁶ This represents a direct comparison of the energy density in 2D and slab turbulence. For example, in the case of the Wind shock event, the ratio of 2D to slab magnetic and kinetic energy density is greater than 1.2 hr upstream and 2 hr downstream of the shock, with approximate values such as $\langle \delta B_{2D}^2 \rangle / \langle \delta B_{\text{slab}}^2 \rangle = 7.14$ (downstream), (upstream), and $\langle \delta u_{2D}^2 \rangle / \langle \delta u_{\text{slab}}^2 \rangle = 103.71$ (downstream); for Ulysses, 3 hr both upstream and downstream of the shock, the corresponding values are $\langle \delta B_{2D}^2 \rangle / \langle \delta B_{\text{slab}}^2 \rangle = 34$ (upstream), $\langle \delta B_{2D}^2 \rangle / \langle \delta B_{\text{slab}}^2 \rangle = 53.4$ (downstream),

⁶ To obtain the total variance of the fluctuating magnetic field and fluctuating velocity field, we first calculate the variances of each component of the magnetic field and velocity field, and then sum them. The perpendicular and slab variances of the magnetic field fluctuations and velocity field fluctuations are calculated from $\sigma_{\text{slab}}^2 = (\sum \langle B_i \rangle S_{ij} \langle B_j \rangle) / \langle B \rangle^2$, and $\sigma_{\perp}^2 = \sigma_s^2 - \sigma_{\text{slab}}^2$ (Belcher & Davis 1971). Here, σ_{\perp}^2 and σ_{slab}^2 denote the variances in the direction perpendicular and parallel to the mean magnetic field $\langle B \rangle$. The averaging $\langle \dots \rangle$ is over a specified time interval, and i, j refer to the R, T , and N components, and σ_s^2 is the trace of \mathbf{S} , where $S_{ij} = \langle A_i A_j \rangle - \langle A_i \rangle \langle A_j \rangle$ is a 3×3 matrix, formed by the R, T , and N component of a vector A .

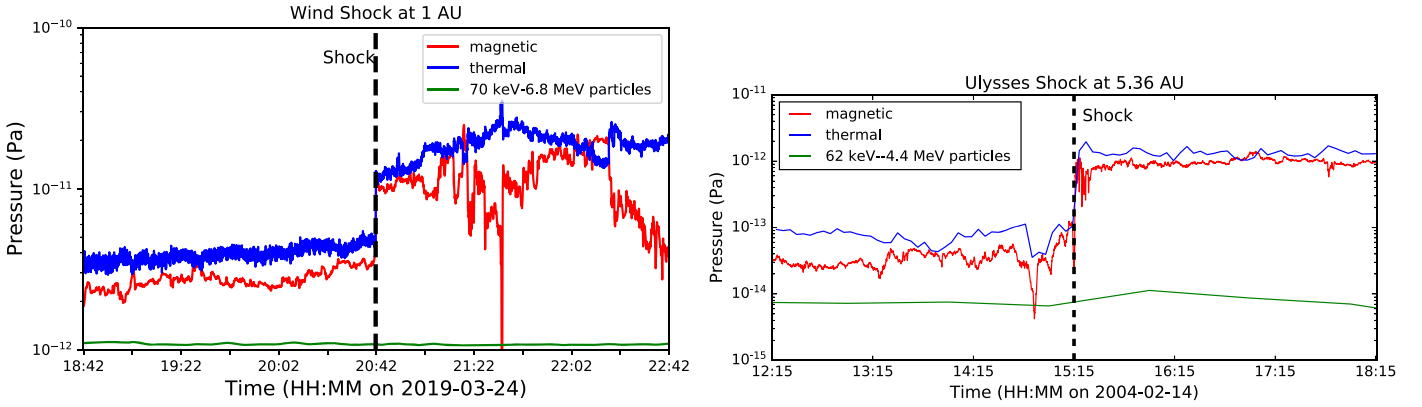


Figure 17. Observations of the total thermal plasma (blue curve), energetic particle (green), and magnetic pressure (red) upstream and downstream of the Wind shock (left panel) and the Ulysses shock (right). The thermal plasma pressure is defined as in MHD and includes the thermal proton and electron contribution. The energetic particle pressure is plotted separately. The vertical dashed line in each panel shows the arrival time of the shock.

$\langle \delta u_{2D}^2 \rangle / \langle \delta u_{slab}^2 \rangle = 17.5$ (upstream), and $\langle \delta u_{2D}^2 \rangle / \langle \delta u_{slab}^2 \rangle = 14.13$ (downstream), and for Voyager 2, $\langle \delta B_{2D}^2 \rangle / \langle \delta B_{slab}^2 \rangle = 3.6$ (upstream), $\langle \delta B_{2D}^2 \rangle / \langle \delta B_{slab}^2 \rangle = 4$ (downstream), $\langle \delta u_{2D}^2 \rangle / \langle \delta u_{slab}^2 \rangle = 3.6$ (upstream), and $\langle \delta u_{2D}^2 \rangle / \langle \delta u_{slab}^2 \rangle = 4.5$ (downstream). These values indicate that the turbulence upstream and downstream of the three shock events are dominated by the 2D component. The Voyager 2 HTS event data was averaged over a 455 day interval and this includes several large amplitude events.

In the theoretical development presented above, we have assumed a large enough plasma beta that the MHD scalar pressure exceeds the magnetic field pressure. In deriving the MHD pressure all possible pressure contributions are included (see the discussion in Zank et al. 2014a), such as the pressures contributed by thermal protons, electrons, and energetic particles. Illustrated in Figure 17 are plots of the thermal plasma pressure (blue curve), energetic particle pressure (green curve), and the magnetic field pressure (red) for the Wind (left) and Ulysses (right) shocks. We plot the energetic particle pressure separately in these figures since their contribution is very small. Evidently, the thermal pressure exceeds the magnetic pressure for both shocks, ensuring that the plasma beta exceeds 1, ranging from about 1.5–3. Finally, the energetic particle pressure, both in the form of the anomalous cosmic-ray component and pickup ions, dominates the upstream thermal and magnetic field pressure at the HTS. This can be seen in Figure 5 of Zank et al. (2018) for the pickup ion contribution, which is significantly larger than the thermal and magnetic pressure contributions, and in Figures 1, 2, and 10 of Florinski et al. (2009), Decker et al. (2008), and Zank (2015), respectively, for the anomalous cosmic-ray proton pressure contribution over the energy range 1–3.5 MeV. At the HTS, the plasma beta, when energetic particles are included, is clearly much larger than 1.

Based on the discussion above about the Wind, Ulysses, and Voyager 2 parameters, we conclude that the underlying assumptions in the analysis are met reasonably well. We can therefore compare the observed downstream spectra for the three shocks shown in Figure 15 to those theoretically predicted with some confidence.

A power spectrum analysis (PSD) is performed for each shock event using different time interval lengths, which represents roughly the inertial range of turbulence at different radial distances. Specifically, the PSD is performed in a 2 hr time interval upstream and downstream of the shock observed

by Wind at 1 au. For the shock event observed by Ulysses at 5 au, the power spectrum is calculated in a 3 hr interval both upstream and downstream. For the Voyager 2 HTS crossing, a 455 day interval is used to compute the spectra. All power spectra are calculated using the standard Fourier analysis with the Blackman–Tukey technique. The Wind data have a resolution of 0.092 s for the magnetic field and 3 s for the velocity and density. The Ulysses data have a resolution of 1 s for the magnetic field and 4–8 minutes for the plasma measurements. The Voyager 2 magnetic field and plasma data have been averaged to a 1 day resolution. The high resolution of the Wind plasma data allows us to investigate the velocity and density fluctuation spectra as well. We show the observed magnetic fluctuation trace spectra upstream and downstream of each shock, and also the transmission of the velocity fluctuation trace spectra and density fluctuation spectra for Wind’s shock in Figures 18 and 19.

The spectra for the magnetic variance are illustrated in Figure 18 for Wind (left panel), Ulysses (middle), and Voyager 2 (right). Each plot contains three spectra. The blue curve is the measured spectrum upstream of the shock, the black curve is the measured downstream spectrum, and the red curve is the theoretical computed downstream spectrum. Based on the parameters listed in Table 1, we used the observed upstream magnetic variance spectrum for the source terms, as done in deriving the spectra in Section 3, to compute the downstream magnetic spectra. The wavenumbers corresponding to the upstream and downstream proton gyroradius k_{g1} and k_{g2} , respectively, are identified by the blue and black vertical lines. The corresponding wavenumbers are off the scale for the Voyager 2 plot.

The comparison of the theoretical and observed downstream magnetic variance spectra for all three examples, Wind, Ulysses, and Voyager 2, is excellent. Both the enhancement in the downstream spectral intensity and the spectral slope are well captured by the theory with the only noticeable discrepancy occurring in the dissipation range of the downstream Ulysses spectrum where there appears to be a little excess power. The Voyager 2 observed downstream spectrum may have a slightly flatter spectrum than that predicted by the theory. However, it is difficult to be completely confident in the accuracy of the observed downstream Voyager 2 spectrum since the 455 day interval over which the spectrum is computed may mean that the plotted spectrum does not accurately represent the magnetic variance spectrum immediately

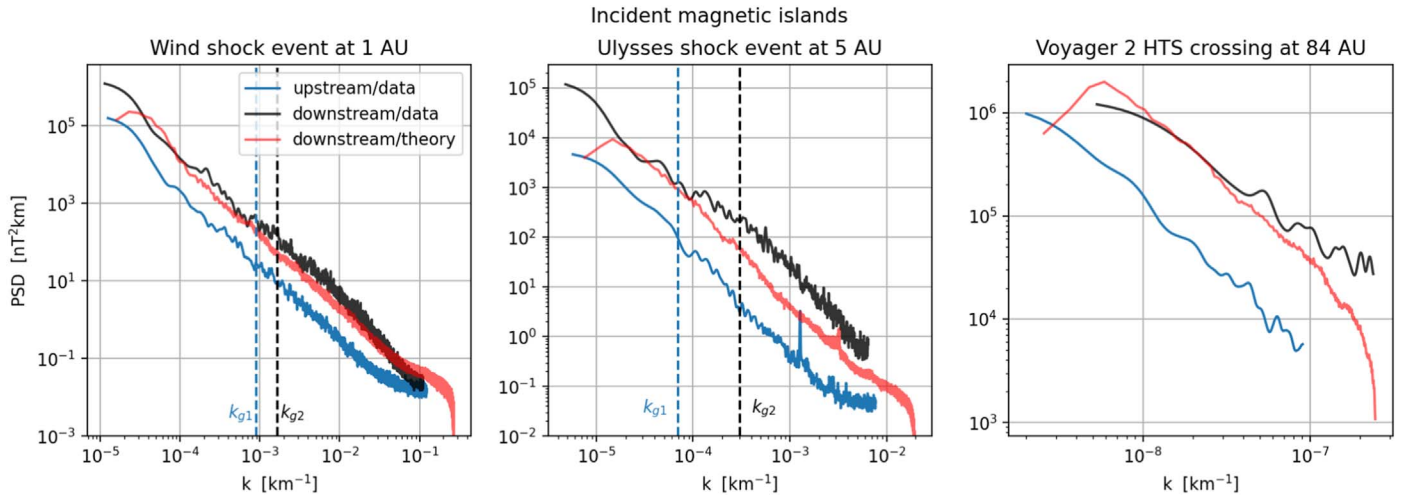


Figure 18. Comparison of the predicted and observed downstream spectrum of the magnetic field variance for the shocks observed by Wind (left panel), Ulysses (middle), and Voyager 2 (right). The blue curve is the spectrum observed upstream of the shock, the black curve is the observed downstream spectrum, and the red curve is the theoretical predicted downstream spectrum. The vertical blue and black dashed lines identify the wavenumber corresponding to the upstream and downstream proton gyroradius k_{g1} and k_{g2} , respectively.

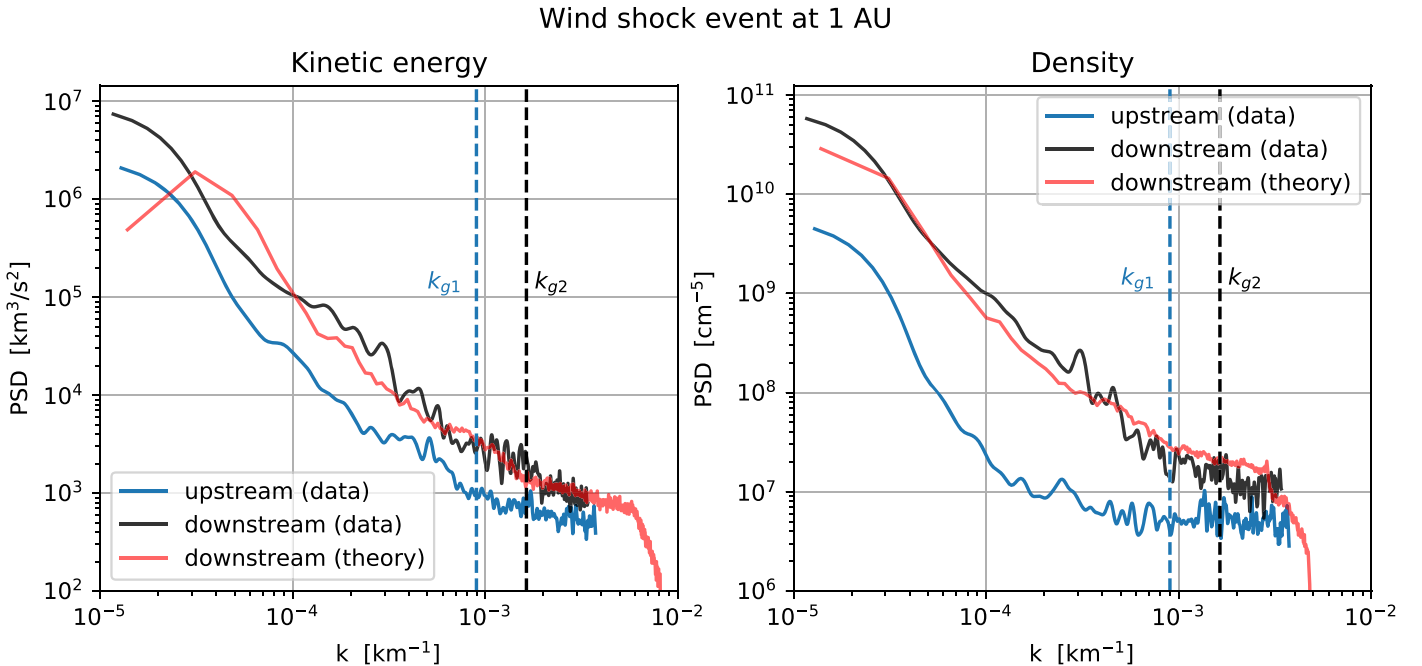


Figure 19. Comparison of the predicted and observed downstream kinetic energy (left) and density variance (right) spectra in the same format as Figure 18 for the Wind shock event.

downstream of the HTS. Nevertheless, the basic theoretical spectral amplitude and index appear to be consistent with observations. Although we have transmitted the spectrum that extends to wavenumbers larger than the upstream gyroradius wavenumber, we note that some care should be exercised in interpreting the high k part of the spectrum. The theory derived here assumes that the shock wave is infinitesimally thin (an idealized MHD discontinuity) but of course, collisionless perpendicular shock waves exhibit structure on gyroradius scales. Consequently, the formal shock-turbulence transmission problem considered here should be restricted to wavelengths that exceed the shock thickness and does not apply to kinetic scales.

Despite the idealized character of the theory and its restriction to magnetic islands, the reason for the good correspondence with the observed downstream PSDs likely stems from the two component nature of solar wind turbulence. In this paradigm, for which there is both theoretical and observational support (Zank & Matthaeus 1992, 1993; Bieber et al. 1996; Forman et al. 2011; Adhikari et al. 2017a, 2017b; Zhao et al. 2017, 2020b; Zank et al. 2017a, 2020; Telloni et al. 2019), solar wind turbulence is a superposition of a dominant quasi-2D component and a minority slab component (the quasi-2D-slab model of NI MHD). The theory of turbulence transmission through a shock wave presented here describes the transmission of the dominant 2D component, and hence it is

not altogether surprising that the theory accounts accurately for the observed downstream spectrum. We comment that we do not find evidence for a steepening of the observed downstream spectrum compared to that upstream, as reported by Borovsky (2020), although we consider only three examples. However, as discussed above, the theory does not suggest that the downstream spectrum should steepen on transmission.

Only the Wind plasma data is of sufficient resolution to allow us to examine the kinetic energy and density variance spectra upstream and downstream of the shock. These spectra are illustrated in Figure 19, using the same format as Figure 18. The theoretical downstream spectra are generated by the observed upstream kinetic energy and density variance spectra. Unlike the magnetic variance case, we must consider Equations (41)–(44) with source terms corresponding to incident vortical fluctuations, incident entropy fluctuations, and incident forward and backward acoustic fluctuations, i.e., a superposition of the source terms used in Sections 2.1–2.3. However, we need to determine the relative contribution of each observational mode to the kinetic energy and density spectra. From the discussion above about the ratio of the 2D to slab energy in magnetic and velocity fluctuations, the Wind ratio of $\langle \delta u_{2D}^2 \rangle / \langle \delta u_{slab}^2 \rangle = 15.96 \sim 16$, which is an interesting value since Zank et al. (2020) argue in Section 2 of that paper that the ratio between the incompressible and NI fluctuations is ~ 4 . Using this ratio as a proxy for the energy in incompressible quasi-2D (vortical) and compressible (acoustic) fluctuations, i.e., vortical kinetic energy/acoustic kinetic energy = 16, and assuming that the acoustic energy is split equally between forward and backward modes, we can decompose the observed upstream kinetic energy and density variance spectra into vortical and acoustic kinetic modes and entropy and acoustic density fluctuations, respectively. Thus, we assume that the upstream velocity and density fluctuations are primarily vortical and entropy (incompressible) modes instead of acoustic (compressible) modes. Such an assumption is consistent with the quasi-2D-slab superposition model discussed above. Bear in mind that the collision of an entropy mode with the shock generates both vortical and acoustic (density) fluctuations as well as amplifying the transmitted entropy/density fluctuations. Similarly, the vortical mode generates both entropy and acoustic (velocity) fluctuations. The theoretical downstream (red curve) kinetic energy spectrum therefore comprises both vortical and acoustic velocity fluctuations, while the theoretical downstream density variance spectrum incorporates both entropy and acoustic density fluctuations. Despite this complicated superposition of transmitted and generated incompressible and compressible fluctuations, the correspondence between the observed kinetic energy and density variance spectra is remarkably good. The theory captures the downstream spectral amplitude and matches the complex non-power-law spectra of both the kinetic energy and density variance spectra. The same comments above regarding the wavenumbers corresponding to the upstream and downstream proton gyroradius apply here.

5. Discussion and Conclusions

Turbulence in the solar wind is modeled frequently as a superposition of a majority 2D and a minority slab component. We have formulated a collisionless perpendicular shock transmission problem in such a way that allows us to study quite cleanly the interaction and transmission of magnetic

islands and quasi-perpendicular fluctuations with a shock wave. The model formulation corresponds to a high plasma beta case in which the mean magnetic field is weak and of the same order in strength as the fluctuating magnetic and plasma variables. In a sense, this represents a strong magnetic turbulence regime. This particular problem, in which the mean magnetic field is orthogonal to the flow and the perturbed flow and magnetic field variables are perpendicular to the mean shock normal (Figure 2), admits a complete separation of gas dynamic and magnetic field components. Acoustic, vorticity, and entropy modes result rather than magnetoacoustic modes because of $\beta_p \gg 1$, and no Alfvén waves are present but instead only advected 2D magnetic islands. Although an idealized formulation of the shock-turbulence transmission problem, it is appropriate to solar wind turbulence because of its superposition of majority 2D and minority slab fluctuations.

We summarize our basic results as follows.

1. The transmission of incident vorticity, entropy, acoustic, and magnetic islands across a perpendicular shock was investigated separately for each mode. For the transmission and generation of non-evanescent downstream plasma modes, the incident vorticity, entropy, and acoustic mode wavenumber propagation angles are limited to a range less than a critical angle $\theta_c^{v,a} < 90^\circ$, otherwise the transmitted and/or generated modes are evanescent and decay in the near field. In a self-consistent treatment, it is likely that the dissipation of the near-field evanescent modes would further heat the plasma immediately downstream of the shock.
2. All incident upstream magnetic island fluctuations are transmitted downstream across the shock regardless of propagation incidence wavenumber angle θ_1 . The amplification of the variance of fluctuating magnetic islands is ~ 10 or less depending on the upstream obliquity of the incident wavenumber θ_1 of the advected $\delta \mathbf{B}_1$ and the shock compression ratio.
3. Depending on the nature of the upstream fluctuation (vortical, entropy, forward, or backward acoustic mode), differences in the properties of downstream transmitted and generated fluctuations exist for each case, particularly in their amplitudes. This is best seen by examining the variances of the transmitted/generated velocity (kinetic energy) and density. For example, a vortical mode incident on a shock generates modest entropic density amplification compared to either an incident entropy mode or acoustic mode. Such an increase in downstream density fluctuations may tie into the observations of downstream *lumpiness* described by Borovsky (2020) who describes observations of an increase in $\delta n/n$ across interplanetary shocks. Although large amplification of upstream density fluctuations can occur with the transmission of an incident acoustic forward and backward acoustic modes, this amplification can probably be discounted since (magneto)acoustic modes are not dominant components typically of solar wind turbulence.
4. The transmission of an upstream mode (advected or propagating) across a shock modifies the k_x wavenumber component, the precise change depending on whether one is considering the transmitted or generated mode. In all cases, except for a very small θ_1 parameter regime for the backward acoustic mode, the k_x wavenumber of the vortical, entropy, and magnetic island modes is increased

quite significantly for $\theta_1 \leq 30^\circ$. By contrast, the acoustic mode k_x wavenumber is scarcely increased on transmission regardless of incident fluctuating mode and that only for some θ_1 values, otherwise $k_{x2} < k_{x1}$. This influences the form of the downstream spectra, particularly the correlation length/bendover scale, for the plasma and magnetic field variables.

5. The transmission of upstream vortical, entropy, forward, and backward acoustic modes, and magnetic islands spectra was investigated. We assumed a simple upstream energy-containing and Kolmogorov inertial range spectrum with a specified correlation length/bendover scale. The transmitted downstream spectrum corresponded to an amplified form of the upstream spectrum (except for the kinetic energy of the backward acoustic mode) in both the energy-containing and the inertial range.
6. The maximum wavenumber of the transmitted vortical, entropic, and magnetic island spectrum is greater than the incident wavenumber, but barely larger for a spectrum of incident forward acoustic modes and slightly less for a spectrum of incident backward acoustic modes. The correlation length is similarly modified.
7. In all cases, the spectral slope of the downstream inertial range of the transmitted spectrum for a specific mode is unchanged from that upstream. The spectra of the corresponding modes generated downstream also have the same spectral slope in the inertial range, whether in the kinetic energy or the density variance.
8. The total kinetic energy and total density variance spectra are a sum of the vortical and acoustic kinetic energy and the entropic and acoustic density variance, respectively. The spectral slopes in the inertial range of each reflect the inertial range of the incident spectrum except for a small, often imperceptible, step in the spectrum because the maximum wavenumber of the incompressible and acoustic modes differ.
9. The amplification of the magnetic energy density spectrum is ~ 10 times in both the energy-containing and inertial ranges (the exact value depending on the shock compression ratio, of course), the bendover scale decreases proportionally, and the spectral form is preserved across the shock.
10. Although the plasma variables and the magnetic field are formally decoupled in the representation considered here, we construct several quantities related to the Elsässer variables, including the normalized residual energy, the normalized cross helicity, Alfvén ratio, and compressibility of the downstream fluctuations. We considered a single case of incident vortical and magnetic island fluctuations with different upstream ratios of residual energy. Despite the upstream compressibility being 0, the downstream fluctuations are modestly compressible, and the downstream normalized residual energy and cross helicity change significantly downstream as a function of the upstream θ_1 .
11. Despite the idealized formulation of the theoretical problem, we apply the theoretical shock-turbulence transmission problem to three shocks observed at 1, 5, and 84 au. In each case, the ordering $B_0 \sim O(\delta B)$ holds and the fluctuating magnetic field component is dominated by the δB_\perp fluctuations, validating the application

of the theory to the observations. Since solar wind turbulence appears to be well described as a superposition of a dominant 2D component and a minority slab component, the approach here allows us to consider the transmission of dominant quasi-2D turbulence across a shock while neglecting the minority component. Accordingly, based on the theory developed here, we took the observed upstream magnetic spectrum and computed the theoretical downstream spectrum, which was then compared to the observed downstream spectrum. The agreement between the theoretically predicted downstream magnetic variance spectrum and that observed was remarkably good, matching both the spectral amplitude for all three cases, and the spectral form and slope very well in the inertial range. Only the shock observed by Wind at 1 au possessed plasma data of sufficient resolution to allow a comparison between theoretical kinetic energy and density variance spectra and observations. The predicted and observed kinetic energy and density variance spectra match extremely well. In decomposing the upstream kinetic energy and density spectra theoretically, we took the observed Wind ratio of quasi-2D to slab energy to motivate the decomposition of the upstream fluctuations into primarily incompressible 2D modes, i.e., magnetic islands, vortical modes (for the kinetic energy spectrum), and entropy modes (for the density spectrum), together with a smaller acoustic component. The ratio of incompressible kinetic energy to compressible was assumed to be 16, consistent with Wind observations and the general theory of NI MHD (Zank et al. 2020). The incompressible upstream modes of course generate compressible velocity and density fluctuations as well as vortical and entropic (incompressible) downstream fluctuations, while also being transmitted downstream. The complicated superposition of these different compressible and incompressible fluctuations yields the theoretically predicted spectrum that results in the very satisfying agreement with observations.

In conclusion, by using a somewhat idealized shock model, we can explore the transmission of quasi-2D turbulence through a collisionless perpendicular shock wave in the large β_p regime. Since quasi-2D turbulence is thought to be the dominant component of low-frequency turbulence in the solar wind, our idealized theoretical model is likely to be quite broadly applicable to shocks in the interplanetary medium. Hence, shocks at widely different heliospheric locations yielded broadly excellent agreement between the theoretically predicted downstream spectra (in terms of intensities and spectral shape) and those observed. The overall theoretically predicted characteristics of the transmission of solar wind turbulence across a collisionless shock appear to be largely consistent with recent observations of shock-turbulence transmission presented by Pitňa et al. (2016, 2021) and Borovsky (2020). This gives us some confidence that (1) solar wind turbulence is comprised primarily of a majority quasi-2D component, and (2) the linear free boundary theory presented here describes accurately the transmission of turbulence across collisionless quasi-perpendicular shocks.

We acknowledge the partial support of a NASA Parker Solar Probe contract SV4-84017, an NSF EPSCoR RII-Track-1 Cooperative Agreement OIA-1655280, a NASA IMAP subaward under NASA contract 80GSFC19C0027, and a NASA award 80NSSC20K1783. We thank the referee for catching an important error and emphasizing the importance of the inertial frame representation.

Appendix A

Rankine–Hugoniot Solutions for the Mean Flow

Here, we list the $O(1)$ expressions for the mean downstream gas dynamic quantities that are needed to compute the downstream fluctuating variables $\delta\Psi_2$. For completeness, we include the jump condition for the weak mean magnetic field, Equation (30). We express $\mathbf{U} = (U_x, U_y) = U(\cos\psi, \sin\psi)$ and define the Mach number as $M_x = U_x/a$ where a is the sound speed. Thus, the various relations that are needed can be expressed in terms of the given upstream Mach number M_{x1} as

$$r = \frac{\rho_2}{\rho_1} = \frac{U_{x1}}{U_{x2}} = \frac{(\gamma + 1)M_{x1}^2}{(\gamma - 1)M_{x1}^2 + 2}; \quad (\text{A1})$$

$$\frac{P_2}{P_1} = \frac{2\gamma M_{x1}^2 - (\gamma - 1)}{\gamma + 1}; \quad (\text{A2})$$

$$\tan\psi_2 = r \tan\psi_1; \quad (\text{A3})$$

$$M_{x2}^2 = \frac{(\gamma - 1)M_{x1}^2 + 2}{2\gamma M_{x1}^2 - (\gamma - 1)}; \quad (\text{A4})$$

$$B_{02}/B_{01} = r. \quad (\text{A5})$$

Appendix B

Transforming into an Equivalent Normal Inertial Frame

It is instructive to cast the oblique shock equations into a form in which the coordinate system moves transversely to the mean shock front. Because the oblique and the transformed system of equations are in equivalent inertial frames, there should be no difference in the results when computing the shock-turbulence transmission problem using one or the other set of equations. This serves as a useful check on the accuracy of the solutions. Since the translation affects only the gas dynamic Rankine–Hugoniot equations, we can begin with the oblique form of the general shock jump conditions, Equations (7)–(10), after neglecting the electromagnetic fields,

$$-\phi_t[\rho] + [\rho u_x] - \phi_y[\rho u_y] = 0; \quad (\text{B1})$$

$$-\phi_t[\rho u_x] + [\rho u_x^2 + P] - \phi_y[\rho u_x u_y] = 0; \quad (\text{B2})$$

$$-\phi_t[\rho u_y] + [\rho u_x u_y] - \phi_y[\rho u_y^2 + P] = 0; \quad (\text{B3})$$

$$-\phi_t \left[\frac{1}{2} \rho u^2 + \frac{P}{\gamma - 1} \right] + \left[\left(\frac{1}{2} \rho u^2 + \frac{\gamma}{\gamma - 1} P \right) u_x \right] - \phi_y \left[\left(\frac{1}{2} \rho u^2 + \frac{\gamma}{\gamma - 1} P \right) u_y \right] = 0. \quad (\text{B4})$$

Use of the Galilean transverse transformation for the constant transverse velocity component U_y

$$x' = x, \quad y' = y - U_y t, \quad t' = t,$$

yields $\partial_x = \partial_{x'}$, $\partial_y = \partial_{y'}$, and $\partial_t = \partial_{t'} - U_y \partial_{y'}$, and hence $\phi_t \rightarrow \phi_{t'}$ and $\phi_y \rightarrow \phi_{y'}$. If we express $u_y = U_y + u'_y$, i.e., effectively a mean and fluctuating part, it is easily seen that

$$-\phi_{t'}[\rho] + [\rho u_x] - \phi_{y'}[\rho u'_y] = 0; \quad (\text{B5})$$

$$-\phi_{t'}[\rho u_x] + [\rho u_x^2 + P] - \phi_{y'}[\rho u_x u'_y] = 0; \quad (\text{B6})$$

$$-\phi_{t'}[\rho u'_y] + [\rho u_x u'_y] - \phi_{y'}[\rho u'^2_y + P] = 0; \quad (\text{B7})$$

$$-\phi_{t'} \left[\frac{1}{2} \rho u^2 + \frac{P}{\gamma - 1} \right] + \left[\left(\frac{1}{2} \rho u^2 + \frac{\gamma}{\gamma - 1} P \right) u_x \right] - \phi_{y'} \left[\left(\frac{1}{2} \rho u^2 + \frac{\gamma}{\gamma - 1} P \right) u'_y \right] = 0, \quad (\text{B8})$$

where $u^2 = u_x^2 + u'_y{}^2$. In the translated frame, Equations (B5)–(B8) have no oblique component and are equivalent to Equations (B1)–(B4).

It is similarly straightforward to transform the corresponding linear wave equations for the acoustic, entropy, and vorticity modes into the primed coordinate system to find that the dispersion relations of each are invariant. However, one can introduce $\bar{\omega} = \omega - U_y k_y$ and rewrite the normal modes as $\delta\Psi' = \delta\hat{\Psi} \exp i[\mathbf{k} \cdot \mathbf{x}' - \bar{\omega} t']$, and $\bar{\omega}' = \bar{\omega} - U_x k_x$ to obtain $\bar{\omega}' = \pm a_0 k$ for acoustic modes and $\bar{\omega}' = 0$ for entropy and vorticity modes with the same eigenrelations as before.

The linear system of equations to be solved for the shock-turbulence transmission problem for an incident vortical mode is given by

$$-(r - 1) \frac{(\bar{\omega}/\omega_0)}{M_{x1}} X_1 + X_2 + r \sin\theta_2^v X_3 - r(M_{x2} \pm \cos\theta_2^a) M_{x2} X_4 = \sin\theta_1^v Y_3; \quad (\text{B9})$$

$$-X_2 - 2r \sin\theta_2^v X_3 + r(1 \pm 2M_{x2} \cos\theta_2^a + M_{x2}^2) X_4 = -2r \sin\theta_1^v Y_3; \quad (\text{B10})$$

$$-\frac{2}{\gamma + 1} (k_y/k_0) \frac{M_{x1}^2 - 1}{M_{x1}^2} X_1 + \cos\theta_2^a X_3 \pm M_{x2} \sin\theta_2^a X_4 = \cos\theta_1^v Y_3; \quad (\text{B11})$$

$$\begin{aligned} & \frac{(\bar{\omega}/\omega_0)}{M_{x1}} \frac{1}{2} (r - 1) \left(M_{x1}^2 + \frac{2}{\gamma - 1} \right) - \frac{2}{\gamma + 1} (M_{x1}^2 - 1) \\ & X_1 - \frac{1}{2r^2} X_2 - \frac{3}{2r} \frac{M_{x2}^2 + \frac{2/3}{\gamma - 1}}{M_{x2}^2} \sin\theta_2^v X_3 \\ & + \frac{1}{r} \left(\frac{1}{2} M_{x2}^2 + \frac{\gamma}{\gamma - 1} \pm \frac{3}{2} \frac{M_{x2}^2 + \frac{2/3}{\gamma - 1}}{M_{x2}} \cos\theta_2^a \right) X_4 \\ & = -\frac{3}{2} \frac{M_{x1}^2 + \frac{2/3}{\gamma - 1}}{M_{x1}^2} \sin\theta_1^v Y_3. \end{aligned} \quad (\text{B12})$$

These equations yield the same results as the oblique system of Equations (41)–(44). The RHS changes according to the incident upstream mode, as in the main body of the text.

ORCID iDs

G. P. Zank  <https://orcid.org/0000-0002-4642-6192>
 M. Nakanotani  <https://orcid.org/0000-0002-7203-0730>
 L. L. Zhao  <https://orcid.org/0000-0002-4299-0490>
 S. Du  <https://orcid.org/0000-0003-1134-3909>
 L. Adhikari  <https://orcid.org/0000-0003-1549-5256>
 H. Che  <https://orcid.org/0000-0002-2240-6728>
 J. A. le Roux  <https://orcid.org/0000-0001-9199-2890>

References

- Achterberg, A., & Blandford, R. D. 1986, *MNRAS*, **218**, 551
 Adhikari, L., Zank, G. P., Hunana, P., et al. 2017a, *ApJ*, **841**, 85
 Adhikari, L., Zank, G. P., Hunana, P., & Hu, Q. 2016a, *ApJ*, **833**, 218
 Adhikari, L., Zank, G. P., Hunana, P., & Hu, Q. 2016b, *JPhCS*, **767**, 012001
 Adhikari, L., Zank, G. P., Telloni, D., et al. 2017b, *ApJ*, **851**, 117
 Anderson, E. J. 2003, *Magnetohydrodynamic Shock Waves* (Cambridge, MA: MIT Press)
 Bamert, K., Kallenbach, R., le Roux, J. A., et al. 2008, *ApJL*, **675**, L45
 Bárta, M., Büchner, J., Karlický, M., & Kotrč, P. 2011a, *ApJ*, **730**, 47
 Bárta, M., Büchner, J., Karlický, M., & Skála, J. 2011b, *ApJ*, **737**, 24
 Belcher, J. W., & Davis, L., Jr. 1971, *JGR*, **76**, 3534
 Bieber, J. W., Wanner, W., & Matthaeus, W. H. 1996, *JGR*, **101**, 2511
 Borovsky, J. E. 2010, *PhRvL*, **105**, 111102
 Borovsky, J. E. 2020, *JGRA*, **125**, e27518
 Borovsky, J. E., & Burkholder, B. L. 2020, *JGRA*, **125**, e27307
 Campeanu, A., & Schlickeiser, R. 1992, *A&A*, **263**, 413
 Cartwright, M. L., & Moldwin, M. B. 2010, *JGRA*, **115**, A08102
 Che, H., & Zank, G. P. 2020, *ApJ*, **889**, 11
 Chen, Y., Hu, Q., & le Roux, J. A. 2019, *ApJ*, **881**, 58
 Chorin, A., & Marsden, J. 1990, *A Mathematical Introduction to Fluid Mechanics*, 175 (Berlin: Springer)
 Decker, R. B., Krimigis, S. M., Roelof, E. C., et al. 2008, *Natur*, **454**, 67
 Du, S., Guo, F., Zank, G. P., Li, X., & Stanier, A. 2018, *ApJ*, **867**, 16
 Du, S., Zank, G. P., Li, X., & Guo, F. 2020, *PhRvE*, **101**, 033208
 Eastwood, J. P., Balogh, A., Dunlop, M. W., & Smith, C. W. 2002, *JGRA*, **107**, 1365
 Eriksson, S., Newman, D. L., Lapenta, G., & Angelopoulos, V. 2014, *PPCF*, **56**, 064008
 Florinski, V., Decker, R. B., le Roux, J. A., & Zank, G. P. 2009, *GeoRL*, **36**, L12101
 Forman, M. A., Wicks, R. T., & Horbury, T. S. 2011, *ApJ*, **733**, 76
 Fraschetti, F. 2013, *ApJ*, **770**, 84
 Giacalone, J., & Jokipii, J. R. 2007, *ApJL*, **663**, L41
 Guo, F., Li, H., Daughton, W., & Liu, Y.-H. 2014, *PhRvL*, **113**, 155005
 Guo, F., Li, S., Li, H., et al. 2012, *ApJ*, **747**, 98
 Guo, F., Li, X., Li, H., et al. 2016, *ApJL*, **818**, L9
 Hu, Q., Ao, X., Peltzer, R., & Zank, G. P. 2012, in *AIP Conf. Ser. 1500, Space Weather: The Space Radiation Environment* (Melville, NY: AIP), 192
 Hu, Q., Zank, G. P., Li, G., & Ao, X. 2013, in *AIP Conf. Ser. 1539, SOLAR WIND 13*, ed. G. P. Zank et al. (Melville, NY: AIP), 175
 Hu, Q., Zheng, J., Chen, Y., le Roux, J., & Zhao, L. 2018, *ApJS*, **239**, 12
 Kallenbach, R., Bamert, K., Hilchenbach, M., & Smith, C. W. 2005, in *AIP Conf. Ser. 781, The Physics of Collisionless Shocks: 4th Annual IGPP International Astrophysics Conference* (Melville, NY: AIP), 129
 Khabarova, O., Zank, G. P., Li, G., et al. 2015a, *ApJ*, **808**, 181
 Khabarova, O., & Zastenker, G. 2011, *SoPh*, **270**, 311
 Khabarova, O. V., & Zank, G. P. 2017, *ApJ*, **843**, 4
 Khabarova, O. V., Zank, G. P., Li, G., et al. 2015b, *JPhCS*, **642**, 012033
 Khabarova, O. V., Zank, G. P., Li, G., et al. 2016, *ApJ*, **827**, 122
 le Roux, J. A., Zank, G. P., Webb, G. M., & Khabarova, O. V. 2016, *ApJ*, **827**, 47
 Li, G., Hu, Q., & Zank, G. P. 2005, in *AIP Conf. Ser. 781, The Physics of Collisionless Shocks: 4th Annual IGPP International Astrophysics Conference*, ed. G. Li, G. P. Zank, & C. T. Russell (Melville, NY: AIP), 233
 Li, G., Miao, B., Hu, Q., & Qin, G. 2011, *PhRvL*, **106**, 125001
 Li, X., Guo, F., Li, H., & Li, G. 2017, *ApJ*, **843**, 21
 Li, X., Guo, F., Li, H., & Li, S. 2018, *ApJ*, **866**, 4
 Lu, Q., Hu, Q., & Zank, G. P. 2009, *ApJ*, **706**, 687
 Luttrell, A. H., & Richter, A. K. 1987, *JGR*, **92**, 2243
 Malandraki, O., Khabarova, O., Bruno, R., et al. 2019, *ApJ*, **881**, 116
 McKenzie, J. F., & Bornatici, M. 1974, *JGR*, **79**, 4589
 McKenzie, J. F., & Westphal, K. O. 1968, *PhFl*, **11**, 2350
 McKenzie, J. F., & Westphal, K. O. 1969, *P&SS*, **17**, 1029
 Moldwin, M. B., Ford, S., Lepping, R., Slavin, J., & Szabo, A. 2000, *GeoRL*, **27**, 57
 Mostafavi, P., Zank, G. P., & Webb, G. M. 2018, *ApJ*, **868**, 120
 Nakanotani, M., Zank, G. P., & Zhao, L. L. 2020, *JPhCS*, **1620**, 233
 Osman, K. T., Matthaeus, W. H., Gosling, J. T., et al. 2014, *PhRvL*, **112**, 215002
 Pitňa, A., Šafránková, J., Němeček, Z., et al. 2016, *ApJ*, **819**, 41
 Pitňa, A., Šafránková, J., Němeček, Z., Durovcova, T., & Kis, A. 2021, *FrP*, **8**, 654
 Pitňa, A., Šafránková, J., Němeček, Z., & Franci, L. 2017, *ApJ*, **844**, 51
 Scholer, M., & Belcher, J. W. 1971, *SoPh*, **16**, 472
 Telloni, D., Carbone, F., Bruno, R., et al. 2019, *ApJ*, **887**, 160
 Vainio, R., & Schlickeiser, R. 1998, *A&A*, **331**, 793
 Vainio, R., & Schlickeiser, R. 1999, *A&A*, **343**, 303
 Yu, W., Farrugia, C. J., Lugaz, N., et al. 2014, *JGRA*, **119**, 689
 Zank, G. P. 2014, *Transport Processes in Space Physics and Astrophysics* (Lecture Notes in Physics), 877 (New York: Springer-Verlag)
 Zank, G. P. 2015, *ARA&A*, **53**, 449
 Zank, G. P., Adhikari, L., Hunana, P., et al. 2017a, *ApJ*, **835**, 147
 Zank, G. P., Adhikari, L., Zhao, L. L., et al. 2018, *ApJ*, **869**, 23
 Zank, G. P., Dosch, A., Hunana, P., et al. 2012, *ApJ*, **745**, 35
 Zank, G. P., Du, S., & Hunana, P. 2017b, *ApJ*, **842**, 114
 Zank, G. P., Hunana, P., Mostafavi, P., et al. 2015, *ApJ*, **814**, 137
 Zank, G. P., Hunana, P., Mostafavi, P., & Goldstein, M. L. 2014a, *ApJ*, **797**, 87
 Zank, G. P., le Roux, J. A., Webb, G. M., Dosch, A., & Khabarova, O. 2014b, *ApJ*, **797**, 28
 Zank, G. P., Li, G., Florinski, V., et al. 2006, *JGR*, **111**, A06108
 Zank, G. P., & Matthaeus, W. H. 1992, *JGR*, **97**, 17189
 Zank, G. P., & Matthaeus, W. H. 1993, *PhFl*, **5**, 257
 Zank, G. P., Nakanotani, M., & Webb, G. M. 2019, *ApJ*, **887**, 116
 Zank, G. P., Nakanotani, M., Zhao, L. L., Adhikari, L., & Telloni, D. 2020, *ApJ*, **900**, 115
 Zank, G. P., Zhou, Y., Matthaeus, W. H., & Rice, W. K. M. 2002, *PhFl*, **14**, 3766
 Zhao, L. L., Adhikari, L., Zank, G. P., Hu, Q., & Feng, X. S. 2017, *ApJ*, **849**, 88
 Zhao, L.-L., Zank, G., Adhikari, L., et al. 2020b, *ApJ*, **898**, 113
 Zhao, L.-L., Zank, G., Adhikari, L., Nakanotani, M., & Telloni, D. 2020a, *A&A*, in press
 Zhao, L. L., Zank, G. P., Chen, Y., et al. 2019a, *ApJ*, **872**, 4
 Zhao, L. L., Zank, G. P., Hu, Q., et al. 2019b, *ApJ*, **886**, 144
 Zhao, L. L., Zank, G. P., Khabarova, O., et al. 2018, *ApJ*, **864**, L34
 Zheng, J., & Hu, Q. 2018, *ApJL*, **852**, L23
 Zhou, X., Büchner, J., Bárta, M., Gan, W., & Liu, S. 2015, *ApJ*, **815**, 6